Sofia University
St. Kliment Ohridski

Application of Coherent Quantum Control Schemes in Classical Physics

Author:
Mouhamad Al-Mahmoud

Supervisor:
Dr. Andon Rangelov

Group of Quantum Optics and Quantum Information
Department of Theoretical Physics

February 2, 2022

Contents

Chapter 1

Introduction

Analogy is a strategy for analyzing and comprehending the world, for gaining insight into various natural occurrences that are connected with similar features or comparable behaviors, and it is thus regarded as the greatest method for transferring thoughts throughout scientific areas [1]. Analogies across diverse disciplines of physics research have proven highly useful in comprehending basic physical principles and the limitations of applicability of various theories.

This dissertation focuses not only on the existence of some quantum-classical analogies between coherent quantum control techniques and some classical systems, but additionally on their applications. The principal goal of these applications is to make these sensitive classical systems as robust and broadband as the quantum systems robustly manipulated by coherent quantum control schemes, especially the composite pulses (CPs). this technique is extensively used in NMR [2–6], quantum optics [7, 8], atomic physics [9–14] and quantum computing [15–23]. The idea of the composite pulses technique is based on the application of a sequence of adjacent radio-frequency (rf) pulses, where each has its own optimized parameters, to manipulate two- and three-state quantum systems. CPs offer the distinct advantage of combining ultrahigh precision with resilience to parameters imperfections, where the pulses sequence acts like a single perfect pulse.

On the other hand, the classical optics systems are known as sensitive in terms of many experimental factors such as the wavelength, the temperature, the medium's properties and the propagation geometric path [24–28]. Two interesting classical systems are the polarization manipulation and the nonlinear frequency conversion. The first takes place when the optical wave passes through an optical element capable of transforming its polarization state. The second is obtained by the passage of the laser beams through a nonlinear crystal. Typically, both systems are sensitive due to the birefringence and several other parameters.

However, *quantum-classical* physics analogy is the key to overcome the sensitivity of these classical systems and many others. First, the notion of CPs technique is adopted to make composite polarization rotator (Chapter 3) and segmented optical parametric amplification (Chapter **??**) that are robust and broadband. Then, the mathematical formalism describing the population transfer in three-state quantum

system via a decaying state can be used to stabilize the spatial powers in cascaded nonlinear frequency generation in dissipative media (Chapter 5). Furthermore, in Chapter 6, we address the design of the nonreciprocal wave retarder, whose retardation depends on the light propagation direction. Finally, Chapter 7 how to build a polarization independent optical isolator whose isolation levels ranging between 43 dB to 50 dB.

Chapter 2

Coherent Quantum Control Techniques

In modern atomic and molecular physics, atoms and molecules prepared in specific quantum conditions are essential not only in connection to studies on dynamic collision or laser-controlled chemical reactions, but also in several new fields. New opportunities have opened up for coherent laser control of the atomic and molecular process by developing selective population transfer schemes, such as the composite pulses (CPs), the rapid adiabatic passage (RAP), and the stimulated Raman adiabatic passage (STIRAP), which are commonly used to manipulate two- and three-state quantum systems. These coherent quantum control techniques are extensively used in NMR [2–5], quantum optics [7, 8, 29], atomic physics [9–13] and quantum computing [15–23]. This manipulation allows an atom or molecule to be efficiently and selectively excited at a certain energy level. The response of the quantum system to incoherent radiation usually leads to an equilibrium excitation, which differs from that of coherent radiation reactions (laser beam), often resulting to entire or partial excitation or population transfer. The two-state and three-state quantum systems, as schematized in the following Fig. 2.1, are the most utilized quantum systems.

In this chapter, we will first introduce two- and three-state quantum systems, and then we will discuss the concept of the Composite pulses techniques and the manipulation of three-state system via a decaying state.

2.1 Composite Pulses

Composite pulses (CPs) technique plays an essential role in the preparation of robust quantum states in several modern physics fields such as NMR, quantum optics, atomic physics, and quantum information [2–5, 7, 8, 11, 13, 18–20, 23, 29]. In NMR, CPs technique is the best option for experiments where a single radio-frequency (RF) pulse isn't enough owing to bandwidth constraints. It was created to manipulate quantum systems (essentially in NMR) and is now frequently utilized to create reliable and efficient quantum gates [16, 17, 20, 22].

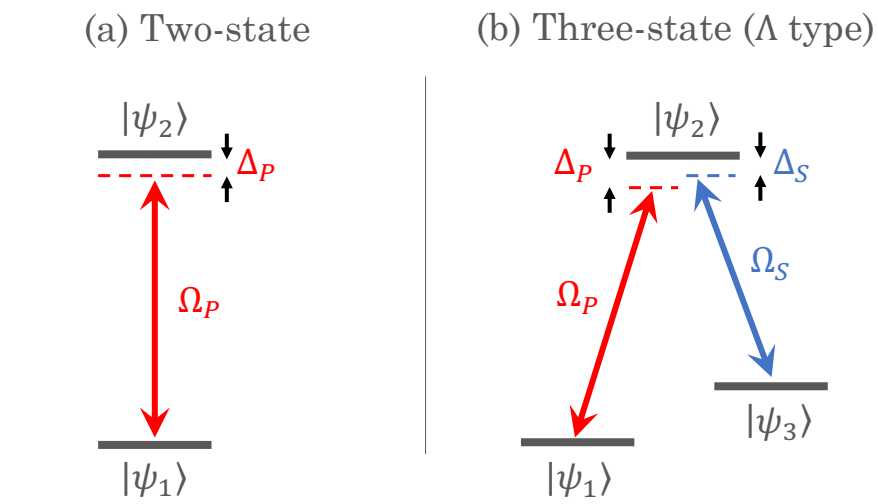

FIGURE 2.1: Schemes of the linkage diagrams of (a) Two-state and (b) Three-state Quantum systems. In both cases, population is initially at the state $|\psi_1\rangle$. Target state is (a) $|\psi_2\rangle$ and (b) $|\psi_3\rangle$. Ω_P and Ω_S are the Rabi frequencies of the pump and the Stokes pulses, respectively. The detunings of Pump and Stokes are depicted by Δ_P and, Δ_S respectively.

2.1.1 Two-state quantum system

A two-state quantum system comprises two energy levels, as shown in Fig. 2.1(a). The population is initially at the ground state ψ_1. By applying a pump field (for example, a laser beam electric field), the system is excited by transferring the population into state ψ_2. Occasionally, such a system could spontaneously decay to state ψ_1 or other energy levels. The parameter $\Delta = \omega - \omega_0$ is called the detuning, which is the difference between the applied laser field frequency ω and the Bohr transition ω_0. The general quantum state of such a system is defined as a linear combination of two states $|\psi_1\rangle$ and $|\psi_2\rangle$ as

$$|\Psi\rangle = \sum_{n=1,2} c_n(t)\,|\psi_n\rangle = c_1(t)\,|\psi_1\rangle + c_2(t)\,|\psi_2\rangle\,, \tag{2.1}$$

where $c_n(t)$ are the probabilities amplitudes. The probability of the quantum state $|\Psi\rangle$ to be in the $|\psi_n\rangle$ is therefore $P_n(t) = |c_n(t)|^2$. The Rabi frequency $\Omega \equiv \Omega_P$ (also known as the frequency of population oscillation) is directly related to the interaction strength and is linked to the transition dipole moment $\vec{d}$ and the electric field $\vec{E}$ as $\Omega = \vec{d} \cdot \vec{E}/\hbar$ When the radiation amplitude fluctuates over time, the pulse area $A(t)$ takes the place of the term Ωt, as

$$\Omega t \rightarrow A(t) = \int_{-\infty}^{t} \Omega(t')dt'. \tag{2.2}$$

Depending on the value of the pulse area $A(t)$, the transfer efficiency oscillates between 0 and 1.

2.1.2 Concept of Composite Pulses

The CPs approach imitates the effect of a single pulse by using a train of contiguous or near contiguous constant amplitude rectangular pulses with a fixed RF frequency and different phases. Among quantum control schemes, CPs has the unique benefit of combining ultrahigh accuracy as resonant techniques with resilience to parameter imperfections as adiabatic passage approaches. Furthermore, CPs allow for the customization of the excitation profile, which is unachievable with a single resonant pulse or adiabatic methods. CPs also feature a built-in compensating mechanism that makes the system more robust. This robustness may be used to overcome common experimental flaws such as the amplitude spread as well as the limited strength of the applied field as compared to spin-spin couplings or molecular electron cloud interactions. The phases of the pulses are set with care to ensure that the composite excitation performs better than a single-pulse excitation. For a coherently driven two-state quantum system, the Schrödinger equation can be written as

$$i\hbar\frac{d}{dt}\mathbf{c}(t) = \mathbf{H}(t)\mathbf{c}(t), \tag{2.3}$$

where $\mathbf{H}(t)$ is the Hamiltonian of the system, and $\mathbf{c}(t) = [c_1(t), c_2(t)]^T$ is a vector column comprising the two probability amplitudes. Unfortunately, this last equation is non-integrable, which means it cannot be solved analytically. We may use an approximation approach known as the Rotating Wave Approximation (RWA) to achieve an analytic approximate solution [30–32]. In the limits of this approximation, the Schrödinger equation describing a coherent excitation in such a quantum system can be expressed as

$$i\frac{d}{dt}\begin{bmatrix} c_1(t) \\ c_2(t) \end{bmatrix} = \frac{1}{2}\begin{bmatrix} 0 & \Omega(t)e^{-iD(t)} \\ \Omega^*(t)e^{iD(t)} & 0 \end{bmatrix}\begin{bmatrix} c_1(t) \\ c_2(t) \end{bmatrix}, \tag{2.4}$$

where Ω is the Rabi frequency, and $D(t) = \int_{t_i}^{t}\Delta(t')dt'$ with $\Delta = \omega - \omega_0$. At resonant excitation ($\Delta = 0$), regardless of the shape of $\Omega(t)$, this Schrödinger equation has a unique analytic solution $\mathbf{U}$. This latter, called the evolution matrix, connects the values of c_1 and c_2 at the final instant t_f to those at the initial moment t_i. It is a propagator of type SU(2), and is parametrized by the complex Cayley-Klein parameters a and b ($|a|^2 + |b|^2 = 1$) [33],

$$\begin{bmatrix} c_1(t_f) \\ c_2(t_f) \end{bmatrix} = \mathbf{U}_\phi\begin{bmatrix} c_1(t_i) \\ c_2(t_i) \end{bmatrix} = \begin{bmatrix} a & be^{-i\phi} \\ -b^*e^{i\phi} & a^* \end{bmatrix}\begin{bmatrix} c_1(t_i) \\ c_2(t_i) \end{bmatrix}. \tag{2.5}$$

where ϕ is a constant phase shift in the Rabi frequency $\Omega \to \Omega e^{i\phi}$. The pulse area $A = \int_{t_i}^{t_f}\Omega(t)dt$ (Eq. 2.2) is the only factor that determines the parameters a and b as, $a = \cos(A/2)$ and $b = -i\sin(A/2)$, with $\Omega(t)$ is assumed to be real, then the

evolution matrix becomes

$$\mathbf{U}_{\phi}(A) = \begin{bmatrix} \cos(A/2) & -ie^{-i\phi}\sin(A/2) \\ -ie^{i\phi}\sin(A/2) & \cos(A/2) \end{bmatrix}. \tag{2.6}$$

The transition probability is $P_{1\to 2} = |b|^2 = 1 - |a|^2$. For a train of N pulses, each with a pulse area A_k and a phase ϕ_k, the overall propagator U^N is obtained by multiplying all the evolution matrices as:

$$\mathbf{U}^N = \mathbf{U}_{\phi_N}(A_N)\mathbf{U}_{\phi_{N-1}}(A_{N-1})...\mathbf{U}_{\phi_2}(A_2)\mathbf{U}_{\phi_1}(A_1). \tag{2.7}$$

The benefit is that all parameters may be freely adjusted to guarantee a reliable and broad population transfer from $|\psi_1\rangle$ to $|\psi_2\rangle$. We define the fidelity $\mathcal{F}$ as the half of the trace of the product of two matrices in order to evaluate the efficiency of the transition, as

$$\mathcal{F} = \frac{1}{2}\left|\mathrm{Tr}\{\mathcal{R}^{-1}\mathbf{U}^N\}\right|, \tag{2.8}$$

where $\mathcal{R}$ is the target matrix describing the ideal excitation. In terms of 2×2 SU(2) matrices, fidelity $\mathcal{F}$ is equivalent to the probability $P_{1\to 2} \equiv P_e$ that quantifies the transfer efficiency.

2.2 Population transfer via a decaying state in a three-state quantum system

In a multi-state quantum system, population dissipation is one of the most limiting factors that reduces population transfer efficiency [34, 35]. The dissipation takes place as a result of a variety of mechanisms, including spontaneous emission, ionization, or collisional relaxation. In three-state quantum systems, in case of a decaying intermediate state, several quantum approaches, such as the Stimulated Raman Adiabatic Passage (STIRAP) and the adiabatic elimination, can be used to overcome this problem and to enhance the transfer efficiency [34]. In this thesis, the quantum-classical analogy is used to profit from dissipation rather than overcome it. To fully grasp this analogy, we first address the concept of a three-state quantum system, then we will discuss the formalism of this problem using the bright-dark basis.

2.2.1 Three-state quantum system

A three-state quantum system (Fig. 2.1(b)) encompasses three states: the initial, the intermediate, and the final states depicted by $|\psi_1\rangle$, $|\psi_2\rangle$ and $|\psi_3\rangle$, respectively. Initially, the population is at the ground state $|\psi_1\rangle$. In order to transfer this population to the target state $|\psi_3\rangle$, two laser pulses, called the pump and the Stokes pulses, are consequently applied. The states $|\psi_1\rangle$ and $|\psi_2\rangle$ ($|\psi_2\rangle$ and $|\psi_3\rangle$) are coupled by the Rabi frequency Ω_P (Ω_S).

The phases $\Omega_P t$ and $\Omega_S t$ must be replaced by two pulse areas $A_P(t)$ and $A_S(t)$ if the amplitudes of radiations fluctuate over time, as

$$\Omega_P(t)t \rightarrow A_P(t) = \int_0^t \Omega_P(t')dt', \tag{2.9}$$

$$\Omega_S(t)t \rightarrow A_S(t) = \int_0^t \Omega_S(t')dt'. \tag{2.10}$$

Because there are two Rabi cycles, the necessary passing through the intermediate state $|\psi_2\rangle$ influences the transfer efficiency, as population may be lost due to spontaneous emission or decay into other states.

2.2.2 *Bright-Dark* basis

In this section, we will explore population transfer in a three-state quantum system via an irreversibly decaying intermediate state with a decay rate Γ, as illustrated by the energy diagram of a Λ-type three-level quantum system in Figure 2.2. As previously

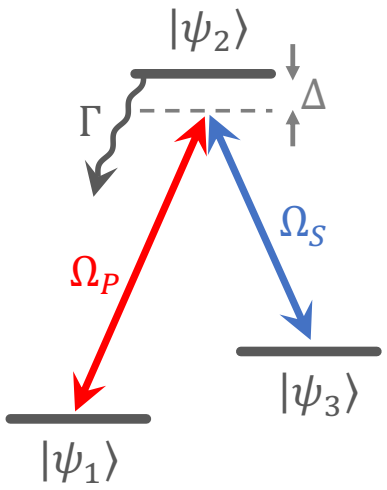

FIGURE 2.2: Energy diagram of a Λ-type three-state quantum system via an intermediate decaying state $|\psi_2\rangle$, whose decaying rate is Γ (s^{-1}). The Rabi frequencies of the pump and the Stokes pulses are depicted by Ω_p and Ω_s, respectively. The intermediate state detunings are assumed to be $\Delta = \Delta_p = \Delta_s$ being the detunings for the pump and the Stokes pulses, respectively.

mentioned in the Section 2.2.1, two optical fields-the pump and the Stokes waves-are required in the three-state quantum system to transfer population from the ground state $|\psi_1\rangle$ to the target state $|\psi_3\rangle$. The pump pulse links states $|\psi_1\rangle$ and $|\psi_2\rangle$, while the Stokes pulse connects the originally unpopulated states $|\psi_2\rangle$ and $|\psi_3\rangle$. The general state of such a system is written as a linear combination of the three unperturbed states as,

$$|\Psi(t)\rangle = c_1(t)\,|\psi_1\rangle + c_2(t)\,|\psi_2\rangle + c_3(t)\,|\psi_3\rangle\,, \tag{2.11}$$

with $c_1(t), c_2(t)$ and $c_3(t)$ being the probability amplitudes of the three bare states $|\psi_1\rangle, |\psi_2\rangle$ and $|\psi_3\rangle$, respectively. In the limit of the rotating wave approximation (RWA) where the rapidly oscillating terms are neglected, the probability amplitudes obey the Schrödinger equation as,

$$i\frac{d}{dt}\begin{bmatrix} c_1 \\ c_2 \\ c_3 \end{bmatrix} = \begin{bmatrix} 0 & \Omega_p & 0 \\ \Omega_p & \Delta - i\Gamma & \Omega_s \\ 0 & \Omega_s & \Delta_p - \Delta_s \end{bmatrix} \begin{bmatrix} c_1 \\ c_2 \\ c_3 \end{bmatrix}. \tag{2.12}$$

The intermediate state detunings of the pump and Stokes pulses, respectively depicted by Δ_p and Δ_s, are assumed to be equal $\Delta = \Delta_p = \Delta_s$; thus the last item of the Hamiltonian matrix is vanished. This system may be treated in either the adiabatic or *bright-dark* basis, however in this section, we will employ the *bright-dark* states basis to depict it. The probability amplitudes of the bright and dark states, respectively denoted by $C_b(t)$ and $C_d(t)$, can be obtained from the probability amplitudes of the bare states via the orthogonal transformation

$$\begin{bmatrix} c_1 \\ c_2 \\ c_3 \end{bmatrix} = \begin{bmatrix} \sin\vartheta & 0 & \cos\vartheta \\ 0 & 1 & 0 \\ \cos\vartheta & 0 & -\sin\vartheta \end{bmatrix} \begin{bmatrix} C_b \\ C_2 \\ C_d \end{bmatrix}, \tag{2.13}$$

where, the mixing angle $\vartheta(t)$ is defined (modulo π) as,

$$\vartheta(t) = \arctan\left[\frac{\Omega_P(t)}{\Omega_S(t)}\right]. \tag{2.14}$$

The intermediate state appears in both bare and *bright-dark* bases. In this context, Eq. 2.12 becomes

$$i\frac{d}{dt}\begin{bmatrix} C_b \\ C_2 \\ C_d \end{bmatrix} = \begin{bmatrix} 0 & \Omega_0 & -i\dot{\vartheta} \\ \Omega_0 & -\Delta - i\Gamma & 0 \\ i\dot{\vartheta} & 0 & 0 \end{bmatrix} \begin{bmatrix} C_b \\ C_2 \\ C_d \end{bmatrix}. \tag{2.15}$$

where $\Omega_0(t) = \sqrt{\Omega_P^2(t) + \Omega_S^2(t)}$ and $\dot{\vartheta}$ depict the effective coupling and the time-derivative of the mixing angle, respectively. In a special scenario, when Ω_P and Ω_S are even constant in time or equal, the mixing angle $\vartheta(t)$ becomes constant, and the time-derivative becomes null, $\dot{\vartheta} = 0$. Therefore, the *dark* state $C_d(t)$ is decoupled from two other states $C_b(t)$ and $C_2(t)$. Thus, the three-state problem is reduced to a two-state system as

$$i\frac{d}{dt}\begin{bmatrix} C_b \\ C_2 \end{bmatrix} = \begin{bmatrix} 0 & \Omega_0 \\ \Omega_0 & -\Delta - i\Gamma \end{bmatrix} \begin{bmatrix} C_b \\ C_2 \end{bmatrix}. \tag{2.16}$$

This equation shows that the effective Rabi frequency Ω_0 connects the *bright* state $C_b(t)$ to the intermediate bare state $c_2(t)$, which decays out of the system with the

decay rate Γ. Because of this coupling, the population that has reached the *bright* state $C_b(t)$ is moved to the intermediate state $c_2(t)$, where it will be eliminated out of the system. Therefore, all the population of this two-state system will be lost after a long interaction period in the case of a large detuning. But because the *dark* state $C_d(t)$ is decoupled from the other states, its initial population is conserved until the end of the interaction.

We adopted this procedure to apply the quantum-classical analogy between this non-Hermitian three-state quantum system and the cascaded nonlinear frequency generation in a dissipative medium. By spatially stabilizing the powers of the interacting waves along the nonlinear crystal, this analogy tries to transform dissipation into advantage. The theoretical concept and results will be examined in detail in Chapter 5.

2.3 Conclusion

In this chapter, we explored the concepts of the Composite pulses (CPs) which is widely used in manipulating two-state quantum systems. Manipulation therefore refers to the effective and selective excitation of an atom or a molecule to a specific energy level. The idea behind CPs is to employ a series of coherent field pulses, each possessing a specific phase and area. In addition, we discussed the problem of a non-Hermitian three-state quantum system with a decaying intermediate state. The bright-dark basis is employed to understand the dynamics of such a system.

Chapter 3

Broadband Composite Polarization Rotator

3.1 Introduction

Components able to convert the polarization state of a light wave are key elements for several optical devices and applications [26, 36–38]. In the case where broadband or tunable light sources are used, a robust and wide bandwidth operation of such components becomes of crucial importance. Methods to realize compact achromatic (broadband) retarders have been therefore the matter of interest for several decades [39–48]. Notably, the recent advances leading to improved broadband performance [44–48] take advantage of the formal analogy between the equations describing the change of polarization in the birefringent plate and the Schrödinger equation for the quantum-state dynamics of coupled two-level systems, pointed out first by Ardavan [44]. The related transfer of concepts allows to apply the fault-tolerant composite pulses approach [2] widely used in the field of nuclear magnetic resonance (NMR) to polarization optics. To this line of ideas belong also the recent studies of achromatic polarization rotators using a stack of several wave-plates [49–51] that we will discuss below.

The most versatile way to realize tunable polarization rotators rely on the combination of several birefringent wave-plates (WPs). It is well known that two half-wave plates (HWPs) with their fast axes making an angle $\alpha/2$ lead to a rotator that turns the polarization by an angle α. In principle, any rotator composed by a combination of WPs should become broadband if every single WP is broadband. Rangelov and Kyoseva [49] have proposed a broadband composite polarization rotator based on the combination of two effective broadband HWPs, each of which is composed by a number of HWPs by the composite approach. The expected device performance was analyzed theoretically in terms of the so-called fidelity (see below) for a total number of HWPs between 6 and 18. This concept was developed further in a recent paper [51], where an even number of HWPs (up to 10) oriented at predetermined angles was used, and the broadband behavior was tested through the transmission of a white light source through an analyzer placed after the HWP stack.

While the above approaches generally require a rather large number of WPs to

achieve a sufficiently broadband operation (≥ 6), in the present work we consider a simplified arrangement involving only three WPs: a full-wave plate between two HWPs. The concept exploits additionally the freedom of rotation of all three elements in the row. It is shown that such a simple stack leads to a broadband polarization rotator provided that the intermediate wave-plate is placed in such a way as to counteract the dispersion of the HWPs. The rotator is robust against the initial polarization direction and the rotation angle can be tuned by rotating only one of the WPs.

3.2 Theory

The broadband polarization rotator proposed in this work is composed of three wave-plate (WP) retarders as shown in Fig. 3.1(a). The first and the third WPs are half-wave plates for the central target wavelength λ_0 of the device, while the intermediate wave-plate is a full-wave plate at the same wavelength. Even though this element leaves the wave unchanged and acts as a neutral element at the wavelength λ_0, the importance of this crucial element for the broadband behavior will become clear below.

As it is well known, a wave-plate retarder is a birefringent element which adds different phases $\varphi/2$ and $-\varphi/2$ to two perpendicular linear polarization components of the light propagating through it. In the framework of Jones calculus [26, 36] and in the LR-basis formed by the Jones vectors for Left and Right circular polarizations, the Jones matrix for a retarder whose fast axis is rotated with an angle θ (with respect to the HV-axes) is given as

$$J_\theta(\varphi) = \begin{bmatrix} \cos\dfrac{\varphi}{2} & ie^{-2\imath\theta}\sin\dfrac{\varphi}{2} \\ ie^{2\imath\theta}\sin\dfrac{\varphi}{2} & \cos\dfrac{\varphi}{2} \end{bmatrix}. \tag{3.1}$$

Here

$$\varphi = 2\pi L(n_s - n_f)/\lambda \tag{3.2}$$

is the wave-plate retardation. The quantities n_f and n_s are the refractive indices along the fast and slow axes, respectively, λ is the vacuum wavelength of the light and L is the thickness of the retarder plate. The most commonly used retarders are the HWPs ($\varphi = \pm\pi$) and the QWPs ($\varphi = \pm\pi/2$). A full-wave plate (FWP) has a retardation of $\varphi = \pm 2\pi$. In addition, the Jones matrix of an axis rotation of an angle α is given as

$$J_R(\alpha) = \begin{bmatrix} e^{-i\alpha} & 0 \\ 0 & e^{i\alpha} \end{bmatrix}. \tag{3.3}$$

For our sequence of HWP-FWP-HWP shown in Fig. 3.1(a) we have $\varphi_1 = \pi$, $\varphi_2 = \pm 2\pi$ and $\varphi_3 = \pi$, the corresponding orientations for the three wave-plates are θ_1, θ_2 and θ_3, respectively. The overall Jones matrix describing this composite

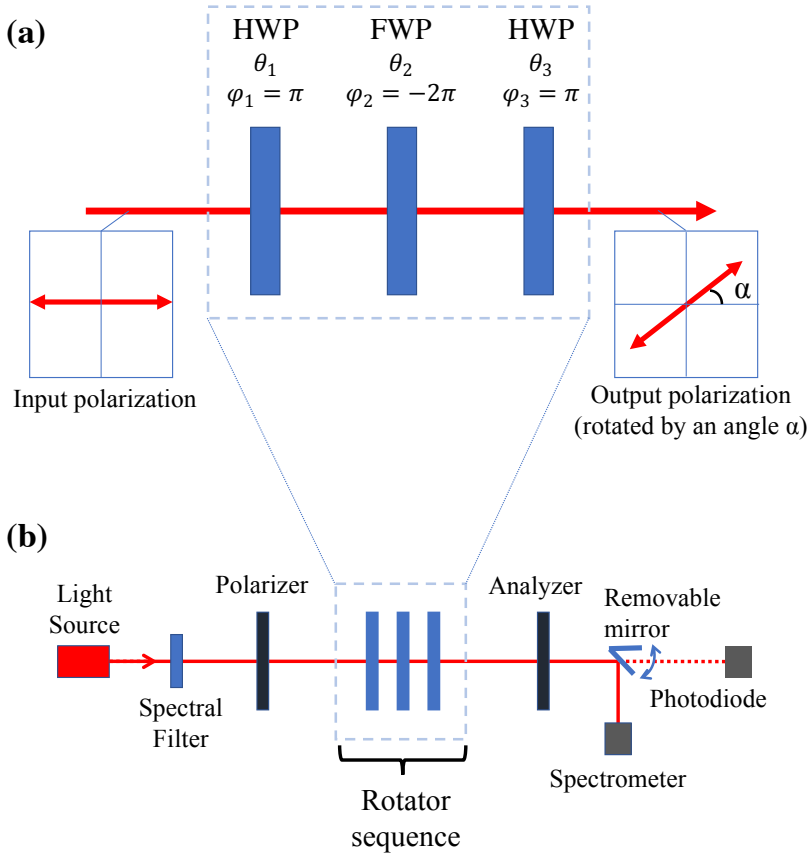

FIGURE 3.1: (a) Principle of the proposed composite polarization rotator composed of three wave-plates, a half-wave plate (HWP) followed by a full-wave plate (FWP) and another HWP. The angles θ_i are the orientation angles of each wave-plate and φ_i are the corresponding retardations. (b) Experimental set-up for the characterization of the composite rotator.

sequence is therefore

$$J = J_{\theta_3}(\pi)\, J_{\theta_2}(\pm 2\pi)\, J_{\theta_1}(\pi)\,, \tag{3.4}$$

which gives

$$J = \begin{bmatrix} e^{-2i(\theta_3-\theta_1)} & 0 \\ 0 & e^{2i(\theta_3-\theta_1)} \end{bmatrix} = \begin{bmatrix} e^{-i\alpha} & 0 \\ 0 & e^{i\alpha} \end{bmatrix}. \tag{3.5}$$

Obviously the last equality shows that J corresponds to the rotator matrix in the LR basis in Eq. (3.3), therefore this sequence acts as a rotator with a rotation angle

$$\alpha = 2(\theta_3 - \theta_1)\,. \tag{3.6}$$

This equivalence is exact at the central wavelength, for which the retardations φ_1, φ_2 and φ_3 correspond exactly to those given above. However, we are principally interested in the behavior found when these retardations depart from the values π, $\pm 2\pi$ and π, as a result of using a different wavelength (see Eq. (3.2)). Therefore, in

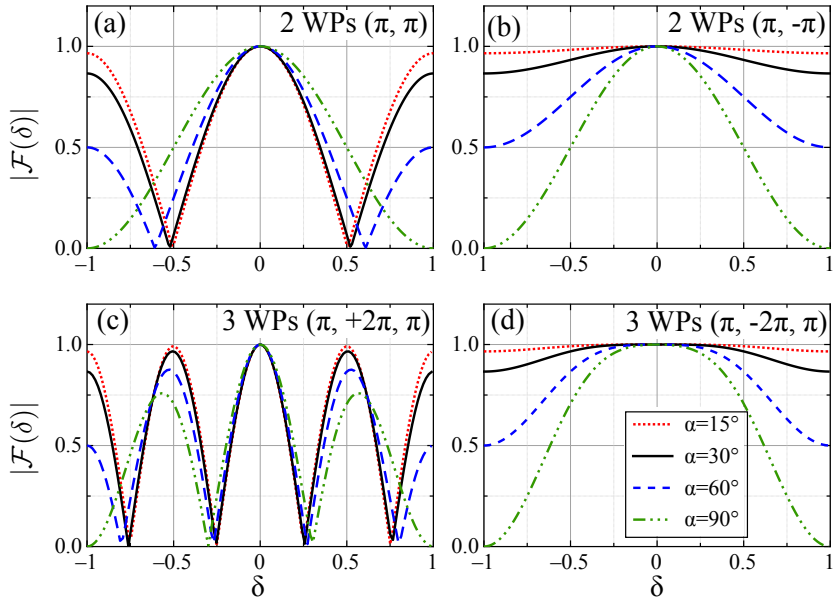

FIGURE 3.2: Absolute value of the fidelity $|\mathcal{F}|$ as a function of the relative retardation deviation δ for four different optical rotator configurations. (a) Two HWP with their fast axes making an angle of $\alpha/2$, equivalent to $\varphi = \pi$ for both wave-plates at the central wavelength. (b) Two HWP with the fast axis of the first making an angle $\alpha/2$ with the slow axis of the second, equivalent to $\varphi_1 = \pi = -\varphi_2$. (c) Three wave-plates, a FWP sandwiched between two HWPs. The fast axis of the FWP makes an angle of $+\alpha/4$ ($-\alpha/4$) with respect to the fast axis of the first (third) waveplate. The retardations are $\varphi_1 = \pi$, $\varphi_2 = +2\pi$ and $\varphi_3 = \pi$. (d) Same as (c) but the fast and slow axes of the FWP are switched (see Eq. (3.9)), here $\varphi_1 = \pi$, $\varphi_2 = -2\pi$ and $\varphi_3 = \pi$. The curves are for following target rotation angles: $\alpha = 15$ deg (dotted red line), $\alpha = 30$ deg (solid black line), $\alpha = 60$ deg (dashed blue line) and $\alpha = 90$ deg (dashed-dotted green line).

order to explore the behavior in the φ space, we define the fidelity factor according to

$$\mathcal{F} \equiv \frac{1}{2} \operatorname{Tr}\left[J_R^{-1}(\alpha)\, J\right], \tag{3.7}$$

where we note that $J_R^{-1}(\alpha) = J_R(-\alpha)$. The fidelity $\mathcal{F}$ is therefore a kind of measure on how close the composite matrix J approaches the target matrix $J_R(\alpha)$. In the case where the output light maintains a linear polarization state, the fidelity $\mathcal{F}$ finds a more direct physical interpretation, as will be mentioned later in the experimental section.

Let us consider the relative deviation δ from the retardation values $\varphi_i = \varphi(\lambda_0)$ of the three wave-plates defined as

$$\delta \equiv \frac{\varphi(\lambda)}{\varphi(\lambda_0)} - 1 = \frac{\Delta n(\lambda)}{\Delta n(\lambda_0)} \frac{\lambda_0}{\lambda} - 1\ , \tag{3.8}$$

where λ_0 is the central wavelength for which the composite structure is designed and $\Delta n = n_s - n_f$ in Eq. (3.2).

While the orientation angles θ_1 and θ_3 are related by Eq. (3.6), the optimum angle θ_2 can be found by maximizing the integral of the fidelity $\mathcal{F}$ over the range $-1 \leq \delta \leq 1$, which means searching for the broadest fidelity curves $\mathcal{F}(\delta)$. It can be shown analytically that this integral is maximized if

$$\theta_2 = \theta_1 + \alpha/4 - \pi/2 = \theta_3 - \alpha/4 - \pi/2 \; . \tag{3.9}$$

The additional angle $\pi/2$ appearing above is important. In fact, the analysis was performed by assuming $\varphi_2(\lambda_0) = +2\pi$, however, the additional angle of $\pi/2$ implies that the role of the slow and fast axis should be permuted for the intermediate FWP, meaning that the optimum is found for a negative retardation $\varphi_2(\lambda_0) = -2\pi$ (by simultaneously dropping the $-\pi/2$ term in Eq. (3.9)).

To illustrate the expected robustness of the composite rotator we depict in Fig. 3.2 the expected fidelity as a function of the relative retardation deviation δ. The quantity being represented is

$$|\mathcal{F}(\delta)| = \frac{1}{2} |\operatorname{Tr}\left[J_R^{-1}(\alpha)\, J(\delta)\right]| \; , \tag{3.10}$$

with

$$J(\delta) \equiv J_{\theta_3}(\pi(1+\delta))\, J_{\theta_2}(-2\pi(1+\delta))\, J_{\theta_1}(\pi(1+\delta)) \, . \tag{3.11}$$

Note that here a unique value of the parameter δ can be considered for the three wave-plates provided that their dispersion is the same, which is the case for the system used in our experimental study. Note also that it is sufficient to consider target rotation angles $|\alpha| \leq 90$ degrees because larger angles are redundant, also the situation for negative angles α is symmetric to the one for positive ones. First we show in Fig. 3.2(a) the standard case where two HWPs under a relative angle $\alpha/2$ are used to create a rotator by an angle α. While such a configuration acts as a perfect rotator at the central wavelength ($\mathcal{F} = 1$ for $\delta = 0$), for all four considered angles α between 15 and 90 degrees the fidelity is found to drop quite quickly as δ departs from zero. This means that such a structure is not spectrally robust. Interestingly, the robustness improves already significantly by means of a small modification, still using only two wave-plates. If the second HWP is turned by an additional 90 degrees, its retardation becomes negative ($= -\pi$) and, as seen in Fig. 3.2(b), the function $\mathcal{F}(\delta)$ remains large over a much wider range of the parameter δ. Figure 3.2(c) show the case where the sequence of Fig. 3.1(a) is implemented with $\varphi_1 = \pi$, $\varphi_2 = +2\pi$ and $\varphi_3 = \pi$. In this case the retardation dispersion associated to the FWP reinforces the dispersion of the HWPs and the fidelity drops even faster than in the case of Fig. 3.2(a). Finally, Fig. 3.2(d) show our chosen configuration for which the orientation angles follow Eq. (3.9) meaning that the slow axis of the FWP is aligned in between the fast axes of the external HWPs. It is evident that in this case the function $\mathcal{F}(\delta)$ gets flatter on the top and is wider than in any other case in Fig. 3.2. As we will discuss later, the experimentally most relevant range for the parameter δ is roughly $-0.5 \leq \delta \leq 0.5$, for which this three wave-plate configuration of Fig. 3.2(d) is clearly outperforming

any other case in Fig. 3.2. It is also worth noting that the curve $\mathcal{F}(\delta)$ is found to be broader for small target rotation angles α than for larger ones. It is worth noting that by using our proposed sequence, the output light maintains its linear polarization. In the next section, we will investigate this configuration experimentally.

3.3 Experiments

The experimental set-up for the characterization of our optical rotator is shown in Fig. 3.1(b). The heart of the system is composed of two crystal polarizers (acting as polarizer and analyzer) surrounding the three wave-plate rotator sequence. The light source is a broadband white light source (Thorlabs SLS201L/M). By inserting the switchable mirror before the detector, the use of the broadband source allows detecting the whole transmitted spectrum through the analyzer with the help of a spectrometer connected to a computer (OceanOptics USB4000-VIS-NIR).

The three wave-plates composing the rotator sequence are realized using three tunable liquid crystal (LC) retarders (Thorlabs LCC1413-A), whose retardations are adjusted with an external applied voltage. The voltage-retardation curve of each of the LC retarder has been priorly calibrated over the spectral range of interest using a Soleil-Babinet optical compensator (Thorlabs SBC-VIS) put in series with the LC retarder and whose mechanically adjustable retardation is known.

We first analyze the behavior of the three-WP rotator at the wavelength λ_0 for which it is designed. The LC wave-plates are adjusted to be half- or full wave-plates at this wavelength. The dependence of the transmitted intensity $I(\beta)$ on the analyzer orientation β (with $\beta = 0$ being the extinction position in absence of the rotator sequence) is $I(\beta) = I_0 \sin^2(\beta - \alpha_{exp}) + I_{min}$, where I_0 is the modulation amplitude and I_{min} is the minimum transmission. Indeed, the degree of linear polarization ξ corresponds to the fringe visibility of such measurements, given by $(I_{max} - I_{min})/(I_{max} + I_{min}) = I_0/(I_0 + 2I_{min})$.

Next, we test the broadband behavior and the robustness of the rotator if the used wavelength differs from the nominal wavelength $\lambda_0 = 550$ nm. First, we send the whole spectrum of the broadband source through the composite rotator and detect the corresponding spectrum after passing the analyzer with the optical spectrometer (see Fig. 3.1(b)). The analyzer is put either in transmission mode (transmitted intensity $= I_{\parallel}$) or in extinction mode (transmitted intensity $= I_{\perp}$). In transmission mode, the analyzer transmission axis is put parallel to the expected output polarization direction under the target rotation angle α for the nominal wavelength, while in extinction mode it is put perpendicular to this direction. For a direct comparison with the theoretically expected intensity, we normalize the intensity $I_{\parallel}$ as $\tilde{I}_{\parallel} \equiv I_{\parallel}/(I_{\parallel} + I_{\perp})$. Figure 3.3 shows the corresponding spectra for $\tilde{I}_{\parallel}(\lambda)$ together with the theoretically expected ones. The latter are obtained by applying the resulting Jones matrix (3.10) to the input polarization Jones vector and projecting the resulting expected output polarization onto the analyzer to obtain the expected transmitted intensity as the

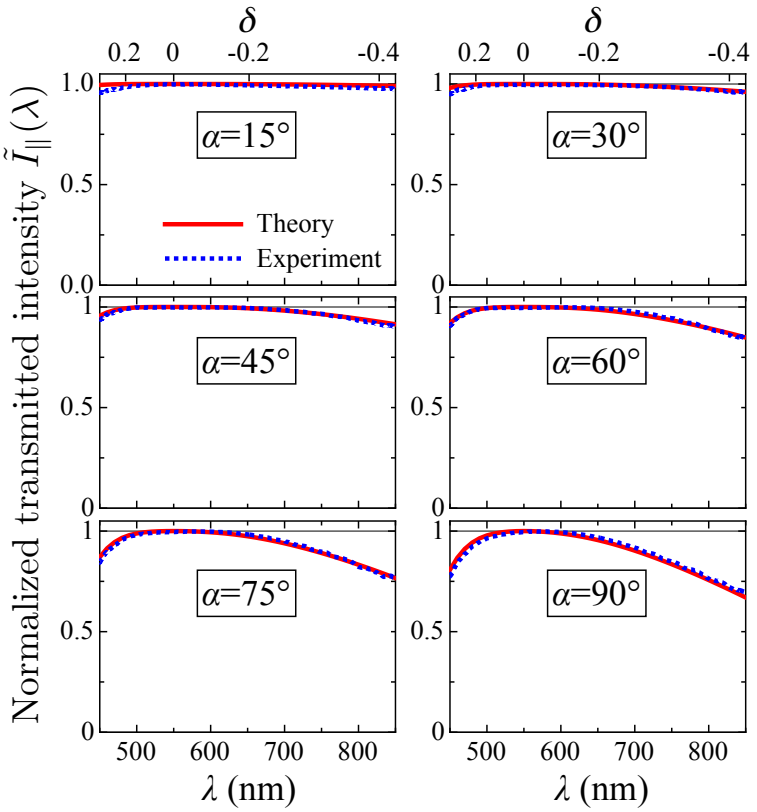

FIGURE 3.3: Normalized transmitted intensity spectra $\tilde{I}_{\parallel}(\lambda)$, the dotted blue curves give the experimental spectra while the underlying solid red lines are the theoretically expected spectra. The nominal wavelength for the three WPs rotator is $\lambda_0 = 550$ nm. The upper scale give the corresponding values for δ.

square of the module of the projected polarization vector. The conversion between the wavelength λ and the relative retardation deviation δ is made by means of

$$\delta(\lambda) = \frac{\lambda_0^2 - \bar{\lambda}^2}{\lambda^2 - \bar{\lambda}^2}\frac{\lambda}{\lambda_0} - 1. \tag{3.12}$$

with an effective oscillator wavelength $\bar{\lambda} = 221.2$ nm. The above expression is obtained by assuming a simplified Sellmeier-like function for the dispersion of the LC birefringence $\Delta n = n_s - n_f$ entering Eq. (3.2). As can be seen in Fig. 3.3, the agreement between the measured and the expected normalized transmission spectra is excellent. Even in the worst case scenario ($\alpha = 90°$ and a wavelength exceeding the nominal wavelength by 300 nm) the normalized transmitted intensity $\tilde{I}_{\parallel}$ is still $\approx 70\%$. A careful analysis shows that, in the case where the output light is still linearly polarized, the normalized transmitted intensity $\tilde{I}_{\parallel}$ corresponds to the square of the fidelity $|\mathcal{F}(\delta)|^2$.

3.4 Conclusion

We have proposed theoretically and verified experimentally a new design for a composite broadband polarization rotator composed of only three wave-plates, two half-wave plates and one full-wave plate for the central nominal wavelength. We have shown that the output polarization state remains nearly linear even for strong departure from the nominal central wavelength λ_0 and that the polarization rotation angle has its maximum at λ_0 and diminishes smoothly away from this wavelength. The rotation angle can be tuned by rotating only one of the wave-plates and is robust against the initial polarization direction. The design presented here is simpler with respect of earlier broadband composite rotators composed of a larger number of wave-plates [49–51].

Chapter 4

Segmented Composite Optical Parametric Amplification

4.1 Introduction

Some optical applications require short optical pulses with large peak power, which may be obtained with the help of optical parametric amplifiers (OPAs) [52–55], that are among the most useful nonlinear optical devices. Optical parametric amplification consists of the nonlinear interaction of three waves. In this process, the two waves at the longer wavelengths—the input signal wave as well as the idler wave—gain power at the expense of the pump wave being at the shortest wavelength. In OPA, the main obstacle encountered when short pulses are used is to combine a high signal amplification and a sufficiently broad amplification bandwidth. The latter is limited because material dispersion imposes that, for a given wave interaction configuration, the exact phase-matching condition can be strictly satisfied only for a single set of wavelengths of the three waves.

In this chapter, we explore a method to achieve broadband amplification bandwidth together with high amplification. The technique involves a combination of quasi-phase-matching (QPM) gratings together with a segmentation of the crystal that implements the equivalent to the composite pulses approach used in Nuclear Magnetic Resonance (NMR) to prepare given quantum states in a robust way [56–58]. The present approach leads to a highly increased robustness of the nonlinear amplification process with respect to both the phase mismatch (associated to a change of wavelength or of temperature) and the coupling strength. Note that the approach presented here does not involve the stretching and chirping of the pulses before the parametric amplification and a final recompression, as used in Optical Parametric Chirped Pulse Amplification (OPCPA) [59–62]. Such steps are generally necessary for the shortest (few cycles) pulses and the highest pulse energies to avoid excessive third order nonlinear effects and/or a damage of the samples.

4.2 Theory

We start with the simmetrized coupled wave equations for collinear three-wave mixing in the slowly varying envelope approximation [24, 63]

$$i\partial_z A_1 = \widetilde{\Omega} A_2^* A_3 \exp\left[-i\Delta k z\right], \tag{4.1a}$$

$$i\partial_z A_2 = \widetilde{\Omega} A_1^* A_3 \exp\left[-i\Delta k z\right], \tag{4.1b}$$

$$i\partial_z A_3 = \widetilde{\Omega} A_1 A_2 \exp\left[i\Delta k z\right], \tag{4.1c}$$

where $\widetilde{\Omega} = -(2\chi^{(2)}/\pi c)\sqrt{\omega_1\omega_2\omega_3/n_1n_2n_3}$ is the effective nonlinear coupling coefficient for first-order QPM, z is the position along the propagation axis, ω_j are the frequencies of the three involved waves, and n_j are their refractive indices. Here $j = 1, 2, 3$ refer to the signal, idler and pump waves, respectively. The quantity $\chi^{(2)}$ in $\widetilde{\Omega}$ is the effective second-order susceptibility and c is the speed of light in vacuum. The amplitudes $A_j \equiv \sqrt{n_j/\omega_j}\, E_j$ in (4.1) are proportional to the amplitudes E_j of the wave electric fields; $|A_j|^2$ is proportional to the number of photons associated to the jth wave. Note that Eq. (4.1) is written in a form that assumes that quasi-phase-matching is implemented and that the quasi-phase matching period is sufficiently short as compared to the interaction length. Therefore, the phase mismatch parameter Δk already contains the mismatch compensation term associated to the periodic grating, that is,

$$\Delta k = k_1 + k_2 - k_3 + 2\pi/\Lambda \equiv \widetilde{\Delta k} + 2\pi/\Lambda. \tag{4.2}$$

where Λ is the quasi-phase-matching period, that is, the first-order local poling period in the case of periodically poled crystals. Obviously, for the central operation wavelengths at which the device is designed, one has $\Delta k = 0$. Concurrently, the true phase mismatch $\widetilde{\Delta k} = k_1 + k_2 - k_3$, which depends only on the wave-vectors k_j of the three interacting waves, is generally quite far from vanishing.

Here, we consider the OPA case, we assume that $\omega_3 = \omega_1 + \omega_2$ and we treat first Eq. (4.1) in the limit of validity of the undepleted pump approximation ($A_3 = \text{const}$). In this limit and for $\Delta k = 0$, we find that both signal and idler increase initially exponentially in a parallel way as

$$|A_1(z)| \approx |A_2(z)| \approx \frac{|A_1(0)|}{2} \exp\left[\Omega z\right] \tag{4.3}$$

In this work, we are interested in an optimization of the signal intensity amplification factor a, defined as

$$a = \frac{|A_1(z)|^2}{|A_1(0)|^2} = \frac{I_1(z)}{I_1(0)}. \tag{4.4}$$

The above argumentation, in connection with Eq. (4.3), indicates that, when the phase-matching condition is satisfied ($\Delta k = 0$), the OPA process is the most efficient. However, this is not entirely true, because the solutions (4.3) are derived only in the limit of the undepleted pump approximation. If one considers the depleted pump

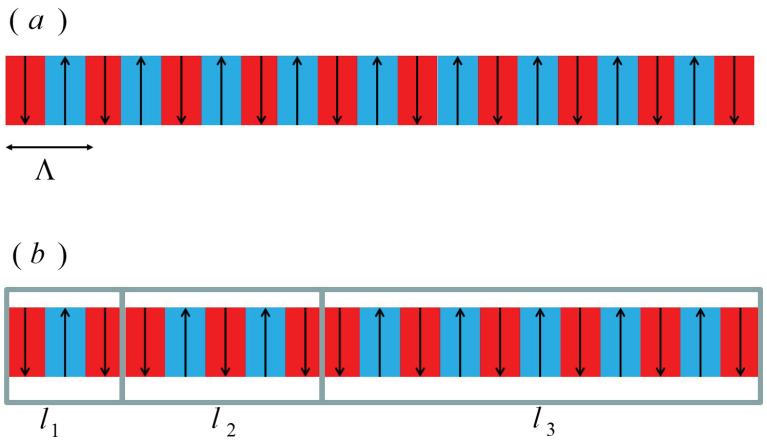

FIGURE 4.1: Sign reversal of $\chi^{(2)}$ nonlinear coefficient for (**a**) standard quasi-phase matching (QPM) technique with local modulation period Λ. (**b**) Composite segmented periodically poled design, with example of 3 segments. All segments are periodically poled with the same period Λ, however once a new segment begins, the sign reversal order of $\chi^{(2)}$ is changed.

regime, the nonlinear Eq. (4.1) has solutions in terms of Jacobi elliptic functions [64, 65]. These, like trigonometric functions, are periodic functions, and thus the energy transfer oscillates back and forth between pump field and signal field.

Here, in analogy with the technique of composite pulses from quantum physics [2, 3, 8, 56–58, 66–68], we propose to use segmented composite crystals for OPA. In the case of OPA, there is no SU(2) symmetry, and it is thus not possible to exploit known composite pulses analytic solutions. Instead, we are going to derive numerically solutions that achieve broadband amplification bandwidth together with high amplification in the depleted pump regime.

4.3 General Numerical Approach and $LiNbO_3$ Crystal Simulations

The procedure that we track is the following. The period of the flip sign of the nonlinear susceptibility $\chi^{(2)}$ is such that the phase mismatch for the OPA process will be zero in Eq. (4.2) due to QPM, resulting in a local modulation period Λ (Fig. 4.1a). Furthermore, at specified boundaries, we introduce further sign flips of the coupling coefficient. In practice, two domains with the same orientation combine at each segment border to form a single double-as-long domain, as shown in Fig. 4.1b. The periodic sign switch of $\chi^{(2)}$ ensures the phase matching for OPA ($\Delta k = 0$) and the additional sign switches of $\chi^{(2)}$ at the segment boundaries will change the sign of $\widetilde{\Omega}$ in the whole crystal segment similarly as in Shaka–Pines pulses from NMR [57, 58]. We denote the intervals between two double length domains as $l_1, l_2, l_3 ... l_N$, as shown in Fig. 4.1b. The determination of the optimum segment lengths l_k is done using Monte Carlo simulations in the depleted pump regime. In practice, it consists

in a maximization of the integral Q of the (normalized) amplification a over a surface of interest in the $(\Delta k, \widetilde{\Omega})$-space, where the values of Δk and $\widetilde{\Omega}$ are in units of the reciprocal crystal length $1/L$. The Figure-of-Merit integral Q is bounded by 1 and is given as

$$Q \equiv \frac{1}{r} \frac{1}{2\widetilde{\Omega}_{max}\Delta k_{max}} \int_{-\Delta k_{max}}^{\Delta k_{max}} \int_{0}^{\widetilde{\Omega}_{max}} a\left(\widetilde{\Omega}, \Delta k\right) \; d(\Delta k) \; d\widetilde{\Omega} \quad , \tag{4.5}$$

where r is the initial pump-to-signal photon-intensity ratio, $r \equiv I_3(0)/I_1(0)$. In our case, we have chosen $\Delta k_{max} = 15/L$ and $\widetilde{\Omega}_{max} = 30/L$, the optimization of the integral Q is done over 10^5 random sets of the segment lengths $l_1, l_2, l_3 ... l_N$. Those corresponding for the best solutions are listed in Table 4.1. We have found that the use of a small number of composite segments (two, three, and partly four) do not lead to any strong improvement with respect to the standard QPM case. In contrast, already, for a moderate number of segments between six and eight, we find a significant improvement of the robustness of the amplification process. In this case, our analysis shows that there are different solutions for the optimum segment configurations (given in Table 4.1), which works better depending on the initial amplitude of the signal wave $A_1(0)$ (as compared to the pump wave amplitude taken as $A_3(0) = 1$).

TABLE 4.1: Numerically found segment lengths l_i (in units of total crystal length L) for composite segmented periodically poled design with N segments. The given values for l_i are such as to optimize the robustness of the OPA process against variations of the nonlinear coupling coefficient and of the phase mismatch Δk.

N	Name	Segment Lengths $l_1; l_2; \ldots; l_N$ in Units of L
3	3	0.373; 0.594; 0.033
4	4	0.303; 0.522; 0.124; 0.051
6	6a	0.293; 0.258; 0.003; 0.255; 0.124; 0.067
6	6b	0.168; 0.035; 0.345; 0.023; 0.222; 0.207
6	6c	0.223; 0.005; 0.404; 0.175; 0.113; 0.080
8	8	0.022; 0.064; 0.046; 0.205; 0.270; 0.096; 0.222; 0.075

In order to prove the concept, we apply it to specific practical examples, and we make the numerics for a real crystal: 5 mol. % Magnesium Oxide doped Lithium Niobate (MgO:$LiNbO_3$). This ferroelectric nonlinear crystal possesses higher damage threshold compared to undoped $LiNbO_3$, high nonlinear optical coefficient, broad transparency range, and is suitable for domain poling [27]. We compare the standard quasi phase matching with the composite approach for OPA when the three interacting beams share the same extraordinary polarisation (Type 0 configuration, all beams polarized parallel to crystal c-axis) associated to the largest element of the nonlinear tensor $d_{333} = \chi^{(2)} = 27$ pm/V.

The color plots in Figure 4.2 illustrate the signal intensity amplification a for MgO:$LiNbO_3$ for standard QPM ($\Lambda = 29.71$ μm) and for a composite crystal made of six segments. It also shows the less optimum case where there are only three composite

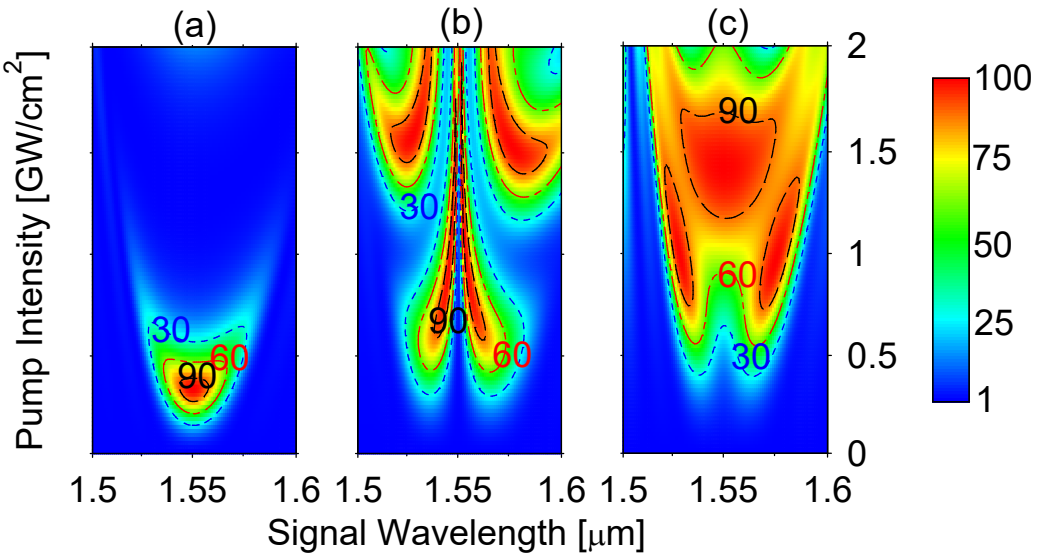

FIGURE 4.2: (Color online) Color plots of the signal intensity amplification a as a function of the input pump intensity I_3 and the signal wavelength λ_1 for the case of MgO:LiNbO$_3$ and with initial conditions $A_1(0) = 0.1$, $A_2(0) = 0$, and $A_3(0) = 1$ so that $r = 100$. The total crystal length is $L = 5$ mm. A pump intensity of 1 GW/cm^2 corresponds to a modified coupling coefficient $\Omega = 1.32$ 1/mm at the central wavelength of 1.55 μm. (**a**) QPM periodic design only. (**b**) Composite crystal with three segments (3 from Table 4.1). (**c**) Composite crystal with six segments (6b from Table 4.1). In all cases, the poling period is Λ =29.71 μm. The color code for the amplification a is given in the color bar on the right-hand side. The three isolines mark intensity amplification levels of 30, 60, and 90.

segments. The nonlinear susceptibility is fixed, and the plots are represented for varying input pump intensity (at the fixed wavelength of 1064 nm) and for varying signal wavelength (with center at $\lambda_1 = 1550$ nm). Note that here, to keep the ratio r constant for each plot, the input signal intensity changes in the same way as the input pump intensity. Note also that the pump intensity (y-axis) takes the role of the coupling coefficient $\widetilde{\Omega}$. Similarly, as a variation of the signal wavelength with respect to the central one gives rise to a phase mismatch Δk; here, the signal wavelength (x-axis) takes the role of Δk. The amplification values are calculated numerically from Eq. (4.1) in the cases when $A_1(0) = 0.1$, $A_2(0) = 0$, and $A_3(0) = 1$. Clearly, a greatly enhanced robustness and frequency bandwidth of the six-segment composite OPA compared to the standard QPM OPA can be recognized.

We can conclude from Figs. 4.2 that the present composite OPA approach works very well in the depleted pump case, because one has a significant pump depletion, and thus a signal amplification approaching the maximum theoretically possible.

4.4 Summary and Conclusions

In summary, we used the similarity between the three wave mixing equations and the time-dependent Schrödinger equation to transfer concepts from quantum physics to nonlinear optics. Specifically, we have suggested to use segmented composite crystals for optical parametric amplification in analogy with the composite pulses in NMR and quantum optics. The approach used here is based on sign-alternating dual-compensating composite pulse sequences similar to those of Shaka and Pines [57, 58]. These are particularly suited for optical parametric amplification because besides the standard quasi-phase-matching they require only additional sign flips of the nonlinear optical susceptibility at specific locations corresponding to the segment frontiers. We have demonstrated numerically that this technique is especially powerful for broad-band OPA. The present approach does not require very long crystals and, for the given example of MgO:$LiNbO_3$, is compatible with pump intensities significantly below the damage threshold for ps or sub-ps illumination [69, 70].

Chapter 5

Cascaded Nonlinear Frequency Conversion in Dissipative Medium

5.1 Introduction

The concepts of coherent quantum control schemes, which are extremely used to robustly manipulate multistate quantum systems, are adopted to make sensitive classical systems robust against the experimental parameters; to name few, Rapid Adiabatic Passage (RAP) in waveguides [71] and the Composite pulses approach in polarization optics (Chapter 3,[72]) and nonlinear optics (Chapter 4, [73]). Another example is the analogy between the three state quantum system and the cascaded two-step nonlinear frequency conversion. Recent researches focused on the usage of the Stimulated Raman Adiabatic Passage (STIRAP) [74–76] and adiabatic elimination [77] in cascaded nonlinear frequency conversion, two simultaneous three waves mixing processes. The three wave mixing processes, such as second harmonic generation (SHG), sum-frequency generation (SFG) and difference-frequency generation (DFG) and others, are generally driven by the second order nonlinear susceptibility $\chi^{(2)}$ in second-order nonlinear crystals and differ by the amplitudes of the input fields [24, 25, 63, 78]. Each parametric process's efficiency is dependent on the conservation of linear momentum of the light, known as phase-matching. To fulfill this condition, the quasi-phase-matching must be used [24, 79–83].

In cascaded nonlinear frequency conversions [84–101], when two processes occur concurrently in the same crystal, phase-matching condition fulfillment becomes more sophisticated and picky. In this situation, two QPM modulation periods must be employed, resulting in aperiodic segmentation.

Almost all the researches which addressed the cascaded nonlinear frequency generation, with or without its analogy with the three-state quantum system, have considered the dissipation as a problem. Moreover, dissipation is not considered obstructive in this work; rather, it is a fundamental feature of the primary subject, in which the damping of the Rabi oscillations is used to stabilize the spatial powers of the interacting waves along the crystal. The main concept is to use a lossy intermediate wave whose frequency is ω_2, while leaving the other waves lossless. By intermediate wave, we mean the one generated during the first process by the interaction of the signal

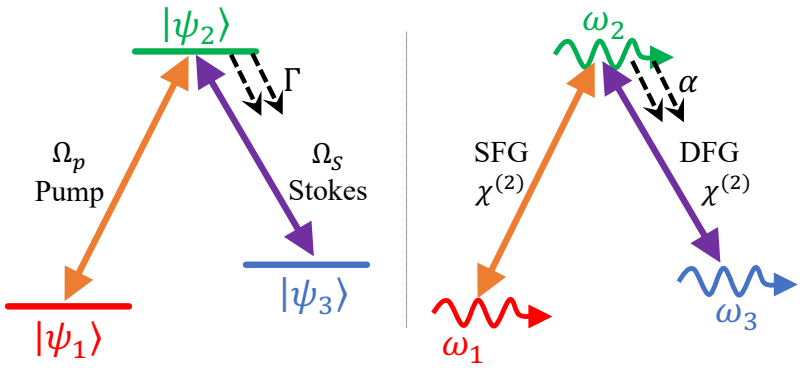

FIGURE 5.1: Diagrams of a Λ-type three-state quantum system (left-frame) and its analogous classical system, the cascaded nonlinear frequency conversion (right-frame). In the left-side diagram, the ground, intermediate, and target states are depicted by $|\psi_1\rangle$, $|\psi_2\rangle$, and $|\psi_3\rangle$, respectively. The two Rabi frequencies Ω_P and Ω_S represent the Pump and the Stokes Rabi frequencies, respectively. In the right-frame, The three frequencies ω_1, ω_2 and ω_3 correspond to the input, intermediate, and target waves, respectively. ω_1 is converted by the sum-frequency generation process (SFG) into ω_2, which is converted, in its turn, into ω_3 by the difference-frequency generation process (DFG). Both processes are driven by the second-order susceptibility $\chi^{(2)}$. Γ (s^{-1}) and α (cm^{-1}) represent the decaying and the absorption rates of $|\psi_2\rangle$ and ω_2, respectively.

(ω_1) with the first intensive pump (ω_{p1}). While this intermediate wave is absorbed with a rate α, it interacts with the second intense pump (ω_{p2}) to generate the target wave (ω_3).

5.2 Theoretical background

The cascaded two-processes nonlinear frequency conversion in a dissipative medium is a classical system that mimics the non-Hermitian three-state quantum system [34] $\{|\psi_{1,2,3}\rangle\,(t)\}$, in which the intermediate state $|\psi_2\rangle$ decays out of the system with a rate Γ (s^{-1}). Generally, in a quantum system, the population is transferred from one state to another as a consequence of the application (presence) of a coherent field, i.e., an electromagnetic radio-frequency electromagnetic field (rf) or a laser beam.

Figure 5.1 presents this analogy between the three-state quantum system (left-frame) and the cascaded two-step nonlinear frequency generation system (right-frame), where the three states $|\psi_1\rangle$, $|\psi_2\rangle$, and $|\psi_3\rangle$ are analogous to the signal, intermediate and target waves whose frequencies are ω_1 ω_2 ω_3, respectively. The time-dependent absorption rate Γ (s^{-1}) and the spatial-dependent one α (cm^{-1}) are analogous. This analogy paves the ground for the usage of the similar mathematical formalism in order to investigate the spatial evolutions of the numbers of photons (photons' fluxes) of the involved waves along the crystal.

To well understand the mathematical formalism behind this analogy, we investigate the case of two simultaneously cascaded processes, for example: SFG followed by a DFG, in a dissipative medium with an absorption constant α for the intermediate state. We assume that three waves are initially injected in the nonlinear medium: a signal (at frequency ω_1), and two intense pumps (ω_{p1} and ω_{p2}), with intensities I_{p1} and I_{p2}, respectively. During the SFG process, the signal wave combines with the first pump to create the intermediate wave $\omega_2 = \omega_1 + \omega_{p_1}$. Simultaneously, the intermediate wave combines with the second pump, by a DFG process. This generates the target wave at frequency $\omega_3 = \omega_2 - \omega_{p_2}$. Due to the dispersion in the nonlinear crystal, the momentum is generally not conserved during the interaction where the phase-mismatches for both SFG and DFG processes are defined as

$$\Delta k_S = k_1 + k_{p_1} - k_2, \tag{5.1a}$$

$$\Delta k_D = k_3 + k_{p_2} - k_2, \tag{5.1b}$$

where $k_j = \omega_j n_j / c \equiv 2\pi n_j / \lambda_j$ is the wave-number of the jth wave whose refractive index and wavelength in the vacuum are depicted by $n_j \equiv n(\omega_j)$ and λ_j, respectively. In the limit of the approximation of the undepleted pumps ($A_{p1,p2} \gg A_1, A_2, A_3$), such a system can be described by the symmetrized coupled wave equations for collinear wave mixing in the slowly varying envelope approximation [24, 25, 63], as

$$i\frac{d}{dz}A_1 = \Omega_S A_2 \exp e^{-i\Delta k_S z}, \tag{5.2a}$$

$$i\frac{d}{dz}A_2 = \Omega_S A_1 e^{i\Delta k_S} + \Omega_D A_3 e^{i\Delta k_D z} - i\alpha A_2,$$

$$i\frac{d}{dz}A_3 = \Omega_D A_2 e^{-i\Delta k_D z}, \tag{5.2b}$$

The amplitudes $A_j \equiv \sqrt{n_j/\omega_j} E_j$ are proportional to the amplitudes E_j of the applied electric fields, and $|A_j|^2$ is proportional to the number of photons Φ_j in the jth wave ($j = 1, p_1, 2, p_2$ and 3). Ω_S and Ω_D depict the effective nonlinear coupling coefficients for the SFG and DFG processes, respectively, expressed as,

$$\Omega_S = 2A_{p1}\frac{d_S}{c}\sqrt{\frac{\omega_1\omega_{p_1}\omega_2}{n_1 n_{p_1} n_2}}, \tag{5.3a}$$

$$\Omega_D = 2A_{p2}\frac{d_D}{c}\sqrt{\frac{\omega_2\omega_{p_2}\omega_3}{n_2 n_{p_2} n_3}}, \tag{5.3b}$$

where $d_S = \chi^{(2)}(\omega_1, \omega_{p_1}; \omega_2)/2$ and $d_D = \chi^{(2)}(\omega_2, \omega_{p_2}; \omega_3)/2$ are the effective second-order nonlinear coefficients. It is interesting to describe this system in the bright-dark basis. To do so, the amplitudes A_j are substituted by the phase-shifted amplitudes

B_j,

$$A_1(z) = B_1(z), \tag{5.4a}$$
$$A_2(z) = B_2(z)\exp\left[i\Delta k_S z\right], \tag{5.4b}$$
$$A_3(z) = B_3(z)\exp\left[-i\left(\Delta k_D - \Delta k_S\right)z\right]. \tag{5.4c}$$

Then, the new amplitudes vector $\vec{B} = [B_1, B_2, B_3]^T$ is transformed into the bright-dark basis $\vec{C} = [C_b, C_2, C_d]^T$ by undergoing the transformation

$$\begin{bmatrix} B_1 \\ B_2 \\ B_3 \end{bmatrix} = \begin{bmatrix} \sin\vartheta & 0 & \cos\vartheta \\ 0 & 1 & 0 \\ \cos\vartheta & 0 & -\sin\vartheta \end{bmatrix} \begin{bmatrix} C_b \\ C_2 \\ C_d \end{bmatrix}, \tag{5.5}$$

where $\vartheta(t) = \arctan(\Omega_S/\Omega_D)$ is the mixing angle. A similar treatment as in Section 2.2.2 leads to a simplified two-state system,

$$i\frac{d}{dz}\begin{bmatrix} C_b \\ C_2 \end{bmatrix} = \begin{bmatrix} 0 & \Omega_0 \\ \Omega_0 & \Delta - i\alpha \end{bmatrix}\begin{bmatrix} C_b \\ C_2 \end{bmatrix}. \tag{5.6}$$

The bright state is tied to the intermediate state, while the dark state is totally decoupled from both of them. According to the presence of the signal wave at the input ($A_1(0) = B_1(0) = 1$ and $A_2(0) = A_3(0) = 0$), we conclude that $C_b(0) = \sin\vartheta$ and $C_d(0) = \cos\vartheta$. The photons, which are initially in the bright state C_b, are transferred to the intermediate state C_2 to be absorbed, while those which are initially in the dark state are conserved ($C_b(L) = 0$ and $C_d(L) = \cos\vartheta$). As a consequence, at the end of the crystal ($z = L$), the amplitudes are $B_1(L) = \cos^2\vartheta$, $B_2(L) = 0$, and $B_3(L) = -\sin 2\vartheta/2$.

The normalized number of photons (photons flux), $\Phi_j(z)$, associated to each wave is defined as $\Phi_j(z) = |B_j(z)|/|B_1(0)|$. In order to have a maximum number of photons at the output, $\Phi_1(L) = \Phi_1(L) = 25\%$, we consider the special case $\vartheta = \pi/4$, that corresponds to equal coupling coefficients $\Omega_S = \Omega_D$. This means that the signal and the target waves will carry each 25% of the initial number of signal photons, while the remaining 50% of the photons initially carried by the bright state is lost as a consequence of the coupling with the decaying intermediate state.

5.3 Example

To validate this analogy, the concept is applied in a lithium niobate ($LiNbO_3$) nonlinear crystal, where the second-order nonlinear coefficients driving both processes are assumed to be equal, as are $d_0 \approx d_S \approx d_D \approx d_{333} = 27$ pm/V [27]. The crystal is supposed to be $L = 25$ mm long and the temperature is $T = 300$K. Its spectrum

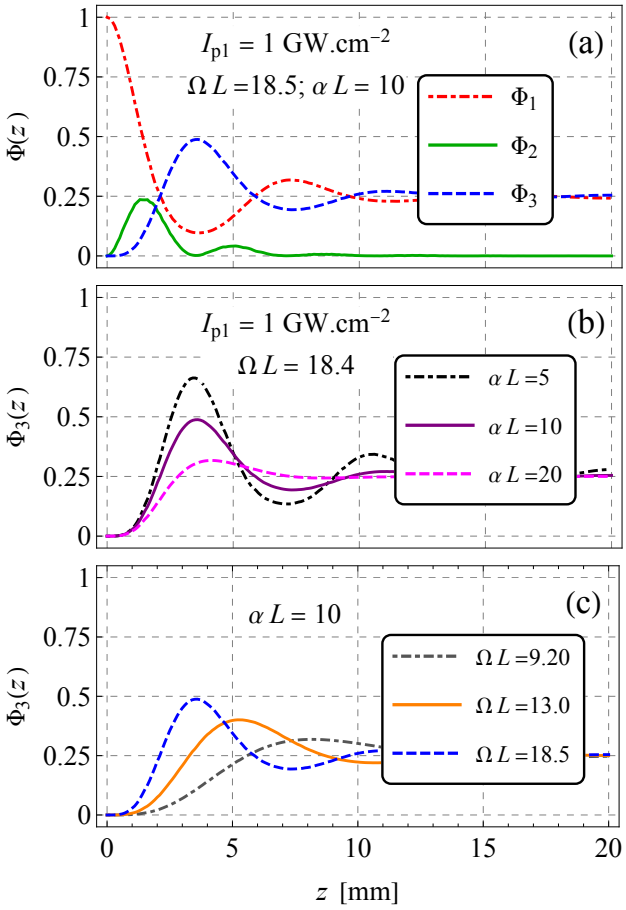

FIGURE 5.2: (a) Spatial evolution of the normalized numbers of photons $\Phi(z)$ associated to the signal (red dotted-dashed curve), the intermediate (green), and the target (blue dashed) waves, as functions of the z coordinates, for $\alpha L = 10$ and $I_{p1} = 1$ GW.cm^{-1} that corresponds to $\Omega L = 18.5$. Panel (b) presents the number of photons $\Phi_3(z)$ of the target wave for $\Omega L = 18.5$ ($I_{p1} = 1$GW.cm^{-2}) for several normalized absorption rates $\alpha L = 5$, 10 and 20. In (c) the normalized absorption is fixed at $\alpha L = 10$, then the evolution of $\Phi_3(z)$ is shown for several values of ΩL =9.2, 13 and 18.5 which correspond to I_{p1} =0.25, 0.5 and 1 GW.cm^{-2}, respectively. For all these cases, the employed second pump intensity is calculated by using the formula $I_{p2} = 0.69 \times I_{p1}$ from Eq. 5.9.

range of absorption is in the UV, then we choose this set of wavelengths:

$$(\lambda_1^{532\text{nm}}) + (\lambda_{p_1}^{800\text{nm}}) \rightarrow (\lambda_2^{319.5\text{nm}}), \tag{5.7a}$$

$$(\lambda_2^{319.5\text{nm}}) - (\lambda_{p_2}^{1064\text{nm}}) \rightarrow (\lambda_3^{456.6\text{nm}}). \tag{5.7b}$$

All the interacted waves are supposed to be polarized in the extraordinary direction. The phase-mismatching relationships belonging to the processes SFG and DFG are $\Delta k_S = k_1 + k_{p1} - k2$ and $\Delta k_D = k_3 + k_{p2} - k2$, respectively. To meet the phase-matching criteria, we employ the Quasi-Phase-Matching (QPM) method. Both phase-mismatches Δk_S and Δk_D are compensated with additional wavevectors $K_S =$

$2\pi m_S/\Lambda_S$ and $K_D = 2\pi m_D/\Lambda_D$, respectively, where m_S and m_D are the QPM orders, and Λ_S and Λ_D are the QPM modulation periods. The corresponding first-order QPM modulation periods for both processes are $\Lambda_S = 1.06$ μm and $\Lambda_D = 1.18$ μm at 300 K. To obtain the maximum value of the number of photons of the target wave, $\Phi_3 = 25\%$, the condition $\vartheta = \pi/4$ must be fulfilled, which requires equal averaged nonlinear coefficients as $\Omega_S = \Omega_D$. In short, the strength of the nonlinearity of the system can be manipulated by two parameters: the correction factor G_m which is connected to the QPM order and the intensities of the pumps. W still need to implement both processes in one crystal so that they can happen at the same time along the crystal. To do so, the crystal must be tuned in such a way that it supports both processes, employing a modulation function $\delta(z)$ [102] defined as

$$\delta(z) = \frac{d(z)}{d_0} = \text{sign}\left[\sin\left(\overline{k}_m.z\right)\sin\left(\Delta k.z\right)\right], \tag{5.8}$$

where, $\overline{k}_m = (\Delta k_S + \Delta k_D)/2m$ and $\Delta k = \frac{\Delta k_S - \Delta k_D}{2}$. The QPM periods are chosen to be $\Lambda_S = 9.6\mu$m and $\Lambda_D = 10.64\mu$m, which correspond to the 9^{th} QPM order, $m = 9$.

Because $\delta(z)$ can contain a number of domains with lengths that are small enough to be difficult to manufacture, we aimed to be prudent by setting the threshold distance at 5 μm. Thus, $\delta(z)$ is corrected by flipping domains of lengths less than 5 μm. Therefore, the nonlinearities of both processes are no longer balanced, then the connection between the pump intensities is

$$\frac{I_{p2}}{I_{p1}} = \frac{n_{p2}}{n_{p1}} \times \frac{n_3.\lambda_3}{n_1.\lambda_1} \times \left(\frac{m_D}{m_S}\right)^2 \times \gamma, \tag{5.9}$$

whith γ is a correction factor ($\gamma \approx 0.8$). The Fourier coefficient for the simultaneous cascaded SFG/DFG processes has the form

$$\overline{G}_m = \frac{1}{m}\left(\frac{2}{\pi}\right)^2. \tag{5.10}$$

The top-frame in Fig. 5.2 depicts the spatial evolutions of the number of photons $\Phi_1(z)$, $\Phi_2(z)$ and $\Phi_3(z)$, which are presented by the red, green and blue curves, respectively, for $\alpha L = 10$. The intensity of the first pump is assumed to be $I_{p1} = 1$ GW.cm^{-2} whose corresponding normalized coupling coefficient $\Omega L = \Omega_S \times \overline{G}_m \times L = 18.5$. By using Eq. 5.9, the corresponding second pump's intensity is $I_{p2} = 0.69$ GW.cm^{-2}. This panel demonstrates that despite the correction of the gratings, the numbers of photons of the signal and the target waves reach 25% of the initial number of signal photons at the input. The panel (b) presents the evolution of $\Phi_3(z)$ for several values of αL with a constant $\Omega L = 18.4$, while (c) illustrates $\Phi_3(z)$ for different ΩL and a constant $\alpha L = 10$.

5.4 Conclusion

In conclusion, we have given a proposal for a cascaded nonlinear frequency conversion in a dissipative medium in which system losses are used to stabilize the spatial powers along the crystal. This system is similar to the non-Hermitian three-state quantum system in that they are both governed by the same mathematical framework.

This study focuses on cascaded SFG-DFG processes, but it does not rule out the employment of other processes, such as DFG-SFG, SFG-SFG, or DFG-DFG. As an example, we discussed the use of a lithium niobate nonlinear crystal as a dissipative medium. Finally, the simulations are in full agreement with the theory.

Chapter 6

Non-reciprocal wave retarder based on optical rotators combination

6.1 Introduction

A conventional wave retarder is generally composed of a transparent birefringent crystal plate inducing a phase shift between the two eigenpolarizations of the plate [26, 36, 103]. They can for instance be used to transform the state of light polarization between linear, circular or elliptical states, as often required in optical experiments and technologies. Being lossless linear optical elements, such retarders are reciprocal owing to the time reversal symmetry connected to the time reversal invariance of the underlying Maxwell equations and of the linear wave equation. Here the reciprocity has the consequence that forward and backward propagating light through the plate are subjected to the same phase shift. However there exist various optical systems capable of breaking reciprocity [104–113].

In this chapter, we propose an approach to realize adjustable non-reciprocal wave retarders on the base of a non-reciprocal Faraday rotator combined to a reciprocal rotator composed of two half-wave plates. It is shown that if these elements are sandwiched between crossed quarter-wave plates they act as wave retarders with a retardation differing in forward and backward direction. The forward and backward phase shifts depend on the combined rotation angle of the rotators and can be adjusted by turning one of the half-wave plates in the reciprocal rotator. Section 2 presents the concept and its theoretical background, while Sect. 3 gives two simple examples of experimental verification using off-the-shelf optical elements.

6.2 Concept background

The principle of the non-reciprocal wave retarder is illustrated in Fig. 6.1(a) for the forward and backward light propagation directions. The two central elements are a reciprocal rotator (RR) turning a linear polarization by an angle θ_1 in forward direction (and turning it back by $-\theta_1$ in the backward direction) and a non-reciprocal Faraday rotator (FR) that turns the polarization by an angle θ_2 for both propagation directions. These two elements are sandwiched between two quarter-wave plates (QWP1 and

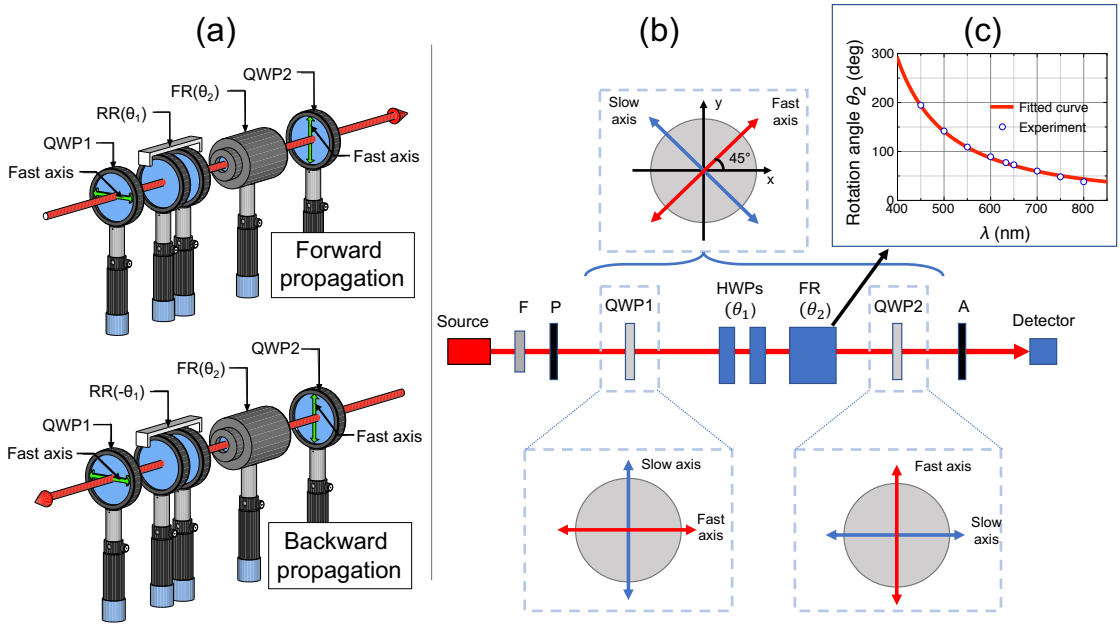

FIGURE 6.1: (a) Non-reciprocal wave retarder sequence for forward (top) and backward (bottom) propagation direction. QWP1 and QWP2 are two crossed quarter-wave plates. RR is a reciprocal polarization rotator (rotation angle θ_1) composed of two half-wave plates (HWPs) and FR is a non-reciprocal Faraday rotator (rotation angle θ_2). (b) Scheme of the set-up for experimental verification. F: spectral filter, P: polarizer, A: analyzer. The bottom diagrams show the orientation of the fast and slow axes of the two QWPs. The top diagram show the 45 deg orientation of the resulting effective retarder having a phase retardation $\varphi_f = 2(\theta_1 + \theta_2)$ and $\varphi_b = 2(\theta_2 - \theta_1)$ in forward and backward directions, respectively. Panel (c) gives the measured dispersion (blue circles) of the rotation angle θ_2 of the FR, as well as the fit with Eq. (6.6) (red curve).

QWP2) with their fast axes aligned along the vertical and horizontal laboratory axes, respectively. The Jones matrix [26, 36] of a waveplate retarder whose axes are rotated by an angle θ with respect to the laboratory axes x and y is written as

$$J_\theta(\varphi) = \begin{bmatrix} e^{i\varphi/2}\cos^2(\theta) + e^{-i\varphi/2}\sin^2(\theta) & -i\sin(2\theta)\sin(\varphi/2) \\ -i\sin(2\theta)\sin(\varphi/2) & e^{-i\varphi/2}\cos^2(\theta) + e^{i\varphi/2}\sin^2(\theta) \end{bmatrix}, \quad (6.1)$$

where $\varphi = 2\pi L(n_s - n_f)/\lambda$ is the retarder phase shift between the fast and the slow polarization components, λ is the wavelength in vacuum, n_f and n_s are the refractive indices along the fast and slow axes respectively, and L is the thickness of the waveplate. On the other hand, the rotation matrix $R(\theta)$ in the horizontal-vertical (HV) basis is given by

$$R(\theta) = \begin{bmatrix} \cos\theta & -\sin\theta \\ \sin\theta & \cos\theta \end{bmatrix}. \quad (6.2)$$

It is well known that a reciprocal polarization rotator can be built by combining two half-wave plates (HWP) for which $\varphi = \pi$ and oriented under the angles θ_A and

θ_B [49, 50]. The corresponding Jones matrix of the RR is obtained directly from (6.1) as

$$\begin{aligned} J_R(\theta_1) &= J_{\theta_B}(\pi)\, J_{\theta_A}(-\pi) \\ &= \begin{bmatrix} \cos[2(\theta_B-\theta_A)] & \sin[2(\theta_B-\theta_A)] \\ -\sin[2(\theta_B-\theta_A)] & \cos[2(\theta_B-\theta_A)] \end{bmatrix} \equiv \begin{bmatrix} \cos\theta_1 & \sin\theta_1 \\ -\sin\theta_1 & \cos\theta_1 \end{bmatrix}, \end{aligned} \tag{6.3}$$

and has, up to a minus sign in the angle, the same form as the rotation matrix (6.2), with a polarization rotation angle $\theta_1 = 2(\theta_B - \theta_A)$.

The combination of the above RR with a FR that rotates further the polarization by an angle θ_2 will lead to a total rotation $\theta_f = \theta_1 + \theta_2$ in forward direction, and to a rotation $\theta_b = \theta_2 - \theta_1$ in backward direction, characterized by the Jones matrices $J_R(\theta_1+\theta_2)$ and $J_R(\theta_2-\theta_1)$, respectively. A tunable polarization rotator can be transformed into a tunable retarder by placing it between crossed QWPs (characterized by the Jones matrix $J_\theta(\pi/2)$). Indeed, the overall Jones matrix J_{seq} for the sequence shown in Fig. 6.1(a) is found as

$$J_{\text{seq}} = J_{\pi/2}(\pi/2)\, J_R(\theta_f)\, J_0(\pi/2) = \begin{bmatrix} \cos\theta_f & -i\sin\theta_f \\ -i\sin\theta_f & \cos\theta_f \end{bmatrix} = J_{\pi/4}(2\theta_f), \tag{6.4}$$

where the last equality can be easily verified by comparing with Eq. 6.1. An equivalent expression (containing the angle θ_b instead of θ_f) holds for the backward direction. It is worth noting that the above transformation is equivalent to the one connecting the rotation gate and the phase gate via the Hadamard gate in quantum information [114]. Equation 6.4 shows that the whole sequence acts as an effective waveplate with two distinct phase retardations in both forward (φ) and backward (φ) propagation directions, as

$$\varphi_f = 2\theta_f = 2(\theta_1+\theta_2), \quad \text{and} \quad \varphi_b = 2\theta_b = 2(\theta_2-\theta_1). \tag{6.5}$$

This effective waveplate is oriented at an angle of $\theta = 45$ deg with respect to the horizontal and vertical laboratory axes and thus also at 45 deg with respect to the orientations of the crossed input and output QWPs. Therefore the arrangement acts as a non-reciprocal waveplate with retardations tunable by the orientations of the internal HWPs. The orientation of the effective non-reciprocal waveplate can be changed by rotating both external QWPs by the same amount in a common direction.

6.3 Experiments

Equations (6.5) show that in principle it is possible to realize any combination of the retardations φ_f and φ_b provided that the rotation angles θ_1 for the RR and θ_2 for the non-reciprocal FR can be adjusted independently. In this section we verify experimentally a specific case where the system acts approximately as a HWP in forward direction and as a QWP in backward direction.

The detailed experimental arrangement is shown schematically in Fig. 6.1(b). The light source is either a broadband white light source (ThorLabs SLS201L) filtered by a spectral filter (F) transmitting a bandwidth $\Delta\lambda = 10$nm (at FWHM) or a He-Ne laser at the wavelength $\lambda = 632.8$ nm without spectral filter. The two HWPs used to realize the RR are built by the combination of two pre-calibrated adjustable liquid crystals waveplates (LCWP, ThorLabs: LCC1421-A) with the applied voltage tuned to a retardation of π for the wavelength of interest. For wavelengths different from 632.8 nm the two QWPs are composed by another LCWP and an optical compensator (ThorLabs SBC-VIS), both tuned to a retardation of $\pi/2$, while for $\lambda = 632.8$ nm two commercial QWPs at this wavelength are used. The used Faraday rotator FR (ThorLabs: IO-3-780-HP) has a central wavelength of 780 nm. We have characterized the dispersion of its rotation angle θ_2 at nine wavelengths between 450 and 800 nm using different spectral filters for the broadband source, as shown in Fig. 6.1(c). Here the experimentally measured rotation angles are fitted by the simplified relation usually applied to the Verdet constant [115, 116]

$$\theta_2 = \frac{A}{\lambda^2 - \lambda_0^2} , \tag{6.6}$$

with $A = 24.7$ deg $(\mu\text{m})^2$ and an effective oscillator wavelength $\lambda_0 = 273.8$ nm. The arrangement in Fig. 6.1(b) corresponds to the forward direction. The backward direction is obtained by interchanging the role of the source and the detector, as well as of the input polarizer (P) and the output analyzer (A).

This sequence acts as a HWP in the forward direction and a QWP in the backward direction for the ideal set of angles $\theta_1 = 22.5$ deg and $\theta_2 = 22.5$deg. For the first demonstration, we choose an input light filtered at the wavelength of 650 nm, for which the measured $\theta_2 = 72$ deg. The rotation angle of the RR was set to $\theta_1 = 26$ deg, this combination leads to a phase shift $\varphi_f = 1.09 \times \pi$ in forward direction and $\varphi_b = 1.03 \times \pi/2$ in backward direction. The input light is horizontally polarized, thus at an angle of 45 deg to the main axes of the resulting effective wave retarder. In order to characterize the function of the sequence we have measured the light extinction characteristics through an analyzer (element A in Fig. 6.1(b), Glan-Thompson polarizer) placed at its output. The normalized transmission through this element for the forward direction is shown in Fig. 6.2(a) together with the predicted theoretical transmission. The latter is obtained by projecting into the analyzer the expected output polarization (obtained by applying the Jones matrix J_{seq} in (6.4) to the input polarization) and taking the square modulus of the result. If the effective retarder would act exactly as a HWP the sequence would rotate the input polarization by 90 deg and lead to a vertically linearly polarized output with perfect extinction when the analyzer is in the horizontal position (angle $\beta = 0$ deg). Here the extinction is not fully complete owing to the 9% excess in phase shift as compared to a HWP resulting from the choice of the angles θ_1 and θ_2. This leads to a slight elliptical component of the output polarization. The normalized transmission for the reversed (backward) direction is shown in Fig.

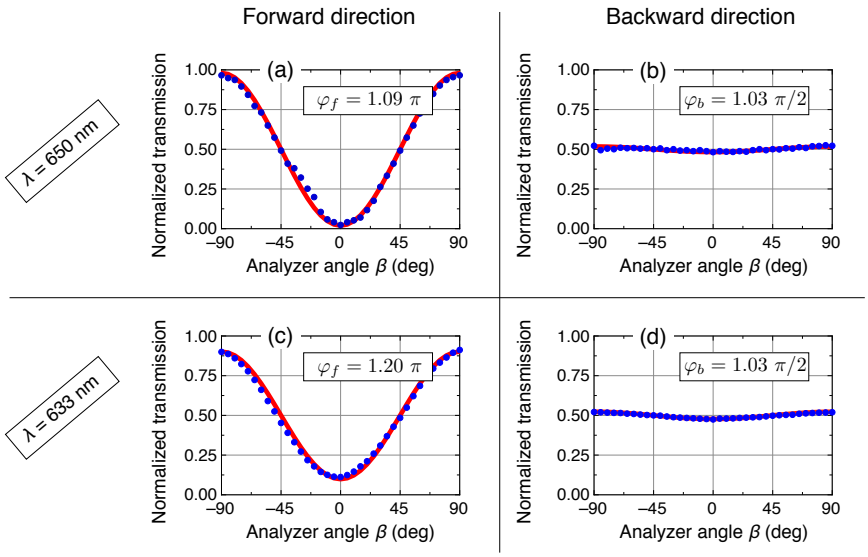

FIGURE 6.2: Normalized transmission through the arrangement of Fig. 6.1(b) as a function of the analyzer orientation angle β for cases where the effective wave plate is close to a HWP in forward direction and close to a QWP in the backward one. Panels (a) and (c) are for the forward direction, (b) and (d) for the backward one. The red curves underlying the measured blue points give the theoretically expected transmission. In (a) and (b) the wavelength λ is 650 nm and the rotators angles are $\theta_1 = 26$ deg and $\theta_2 = 72$ deg, leading to phase shifts of $\varphi_f = 1.09\ \pi$ and of $\varphi_b = 1.03\ \pi/2$. In (c) and (d), $\lambda = 632.8$ nm, $\theta_1 = 30.9$ deg and $\theta_2 = 77.3$ deg, so that $\varphi_f = 1.20\ \pi$ and $\varphi_b = 1.03\ \pi/2$. The angle β is given with respect to the polarizer orientation which defines the input polarization, for $\beta = 0$ polarizer and analyzer are parallel.

6.2(b). Also here the measured and theoretical transmission agree well and a value close to the β-independent 50% level expected for the circular polarized output of an ideal effective QWP is verified.

If the above experiment is repeated with the 632.8 nm He-Ne laser wavelength the results are very similar. In this case the non-reciprocal rotation angle is $\theta_2 = 77.3$ deg. The corresponding experimental and theoretical normalized transmitted powers obtained upon choosing an angle $\theta_1 = 30.9$ deg for the RR are shown in Fig. 6.2(c) and 6.2(d) for the forward and backward directions, respectively. In this case the forward phase shift is $\varphi_f = 2\theta_f = 1.20 \times \pi$ and the backward phase shift is still $\varphi_b = 1.03 \times \pi/2$ close to a QWP. The comparison of Fig. 6.2(a) with Fig. 6.2(c) confirms that at 632.8 nm the structure in forward direction departs more from an effective HWP, what results in a stronger elliptical component of the output polarization and a smaller modulation of the transmission upon rotation of the analyzer. Indeed, the degree of linear polarization ξ corresponds to the fringe contrast of such a measurement [117] and decreases in forward direction from 96% to 80% going from the case of Fig. 6.2(a) to the one of Fig. 6.2(c).

6.4 Discussion and conclusions

We have presented a universal design of a non-reciprocal wave retarder based on a combination of a reciprocal and a non-reciprocal polarization rotator with two quarter-wave plates. The proof-of-concept was successfully verified experimentally for a few useful cases. The phase shifts in forward and backward directions can be adjusted by varying the reciprocal and non-reciprocal rotation angles θ_1 and θ_2. In our tests the reciprocal rotator was implemented by using a pair of half-wave plates. It is worth noting that this pair of elements may be replaced by a plate of an optically active crystal such as quartz, at the expense of a loss of tunability of the angle θ_1. The presently proposed design can find applications whenever a different manipulation of the light polarization state in two opposite directions is of interest. For instance, polarimetric analysis can take advantage of injecting the same input polarization state on both opposite ports, permitting to duplicate polarization manipulation and analysis in a single device. Novel types of optical isolators or circulators can also be envisaged. Furthermore, since for polarization encoded q-bits wave plates can take the role of various quantum gates [114], the present approach may be used also to realize different quantum optical gates in a single device, for instance an X gate in one direction and a Hadamard gate in the other. Finally, by exploiting the dispersion of the underlying reciprocal and non-reciprocal elements, new types of coarse wavelength sensors based on the differential response in the two directions may be conceived.

Chapter 7

Polarization Independent Optical Isolator in Sagnac-Type Configuration

7.1 Introduction

An optical isolator is a device that allows the light to pass in one direction but blocks it in the other. The first optical isolator (OI) was suggested by Rayleigh [118] and consists of a Faraday rotator sandwiched between two polarizers. Using this main principle, simple schema were realized by using different type of polarizers optimized for specific spectral regions, optical power levels, or for the pulsed rather than the continuous wave regime.

The major drawback of Rayleigh's optical isolators is to work in an optimum way only for one specific input light polarization that should be known in advance. The same is true also for most recent magneto-optics-based isolators developed in integrated photonics, where either the TM or the TE polarization is generally being addressed (see [119–123] and references therein). Disposing of optical isolators operating independently of the state of the incoming light polarization is an attractive feature for both bulk optics and integrated implementations. Different strategies have been developed to this aim, such as using birefringent plates [124–127] or Mach-Zehnder interferometers in waveguide configurations [128–130]. Finally, various types of polarization independent circulators were developed either on a bulk optics [131–140] or an integrated platform [121, 141–143].

Here we propose an alternative way to realize a polarization independent optical isolator (PIOI) based on a common path interferometer and verify its proof of principle in a bulk optics arrangement. The optical design is based on a Sagnac-type interferometer, with the ring containing two nonreciprocal polarization switches (NRPS) put in series and intercalated by a polarizer. The NRPSs are composed of a Faraday rotator and a half-wave plate and leave the polarization unchanged for propagation in one direction but switches it between horizontal and vertical (rotation by 90 deg) in the opposite direction. Importantly, in our PIOI the two orthogonal polarizations

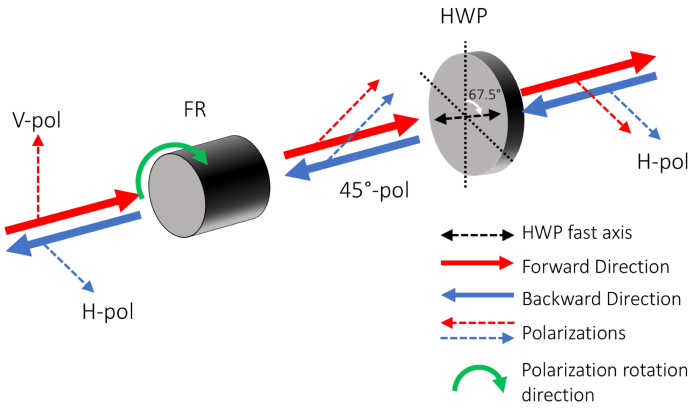

FIGURE 7.1: (Color online) Principle of the nonreciprocal polarization switch (NRPS). FR is a Faraday rotator with 45 deg rotation angle and HWP is a half-wave plate oriented at 67.5 deg.

are treated simultaneously. They follow the same path within the ring but in counter propagating directions.

7.2 Concept

The principles underlying the NRPS and the PIOI are illustrated in Fig. 7.1 and Fig. 7.2, respectively. The NRPS is composed of a Faraday rotator (FR) and a half-wave plate (HWP). The FR, as a non-reciprocal element, rotates the light polarization by 45 deg in the same direction for both light propagation directions and for all polarizations. In contrast, the HWP with one of its main axes oriented at 67.5 deg, rotates the polarization by +45 deg in the forward direction and by -45 deg in the backward one, provided that the input polarization is either horizontal or vertical. The overall effect of the NRPS is therefore to impose a 90 deg polarization rotation in forward direction (switch between the horizontal and vertical polarizations) and to leave the polarization unchanged in the backward one (see Fig. 7.1).

The PIOI working principle is illustrated for the specific cases of a vertical and horizontal input polarization in Fig. 7.2(a) and Fig. 7.2(b), respectively. Any light beam (red arrows) entering through the port 1 will exit the PIOI at port 2 with the same polarization as the input light. On the other hand, if the light (blue arrows) re-enters the PIOI through port 2 in backward direction, due to the effect of the NRPSs the polarization is rotated in such a way that the whole wave is blocked by the horizontal polarizer (P) in the ring, so that no light can exit from port 1 in backward direction.

In summary, a forward input wave with arbitrary polarization is splitted by the PBS in its vertical polarization component (traveling clockwise through the ring) and its horizontal components (traveling counter-clockwise). Both will exit through port 2 after propagation through an equal path length in opposite directions. A backward wave from port 2 is also splitted by the PBS. However, in this case the

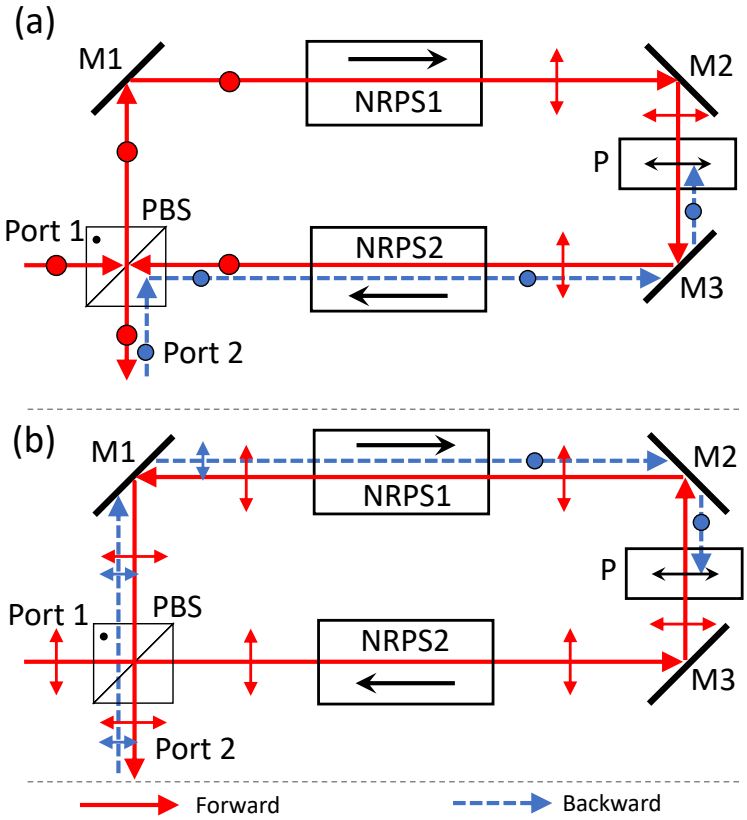

FIGURE 7.2: (Color online) Polarization-independent optical isolator design (PIOI). In forward direction (red-solid arrows), the light travels from port-1 to port-2. In backward direction (blue-dashed arrows), the light traveling from port-2 towards port-1 is blocked at the horizontal polarizer (P). Frames (a) and (b) correspond to vertical and horizontal input polarizations, respectively. PBS is a polarizing beam splitter, NRPS1 and NRPS2 are nonreciprocal polarization switches as of Fig. 7.1, and M1-M3 are mirrors.

vertical component travels counter-clockwise and the horizontal travels clockwise until reaching the polarizer and being blocked.

7.3 Experiments

Experimental proof of the proposed concept is realized by means of a bulk optics set-up corresponding to the design of Fig. 7.2. All experiments were performed with a cw Ti:Sapphire laser adjusted to the wavelength $\lambda = 798$ nm. Both Faraday rotators (IO-3-780-HP, Optics for Research) in the NRPSs were also tuned to have 45 deg rotation at this wavelength. Two electrically tunable liquid crystals retarders (Thorlabs LCC1413- A) were calibrated to have the role of two HWP at this wavelength and their fast axes were rotated by 67.5 deg with respect to the vertical direction as shown in Fig. 7.1.

In order to prove that the PIOI conserves the input polarization, we quantify the transmitted intensities by an analyzer followed by a silicon photodetector. In

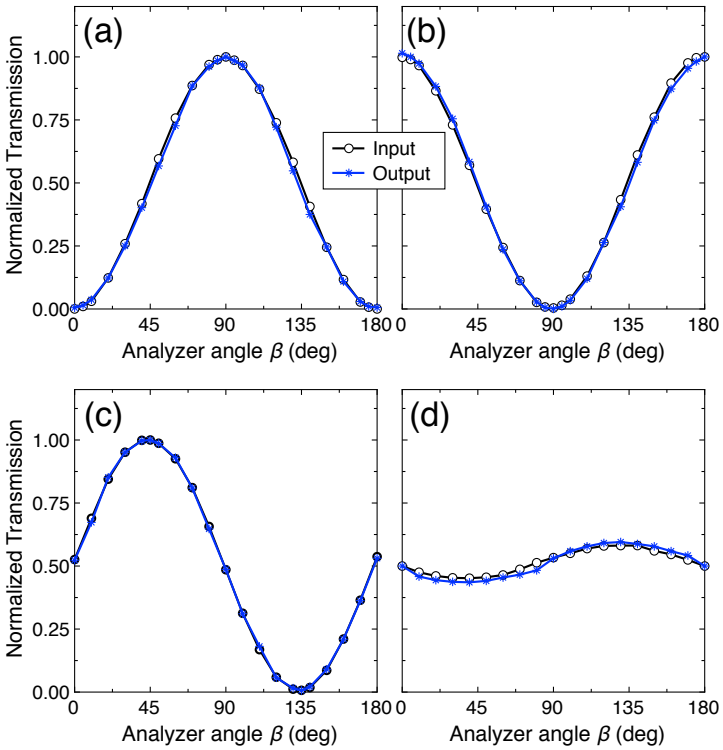

FIGURE 7.3: (Color online) Normalized transmission power through an analyzer for four different input polarization states: (a) horizontal, (b) vertical, (c) linear at nearly 45 deg and (d) elliptical. Measurement are for the forward direction through the PIOI. The black circles are measured at the input (before Port-1) and the blue stars at the output (after Port-2). The curves overlap confirms the conservation of the polarization state.

forward direction, these were inserted alternatively before Port-1 and after Port-2. The normalized transmitted power upon rotation of the analyzer were taken in both cases. The results are shown in Fig. 7.3 for four different states of input polarization: horizontal, vertical, linear at nearly (but not exactly) 45 deg and elliptical. The good overlap between the curves for the input and the output confirms the conservation of the polarization. For the four states of polarization used for Fig. 7.3 we also evaluated the back-reflection losses η from the PIOI. The latter are defined as $\eta(dB) = 10\log_{10}[P_{input}/P_{back}]$, where P_{input} and P_{back} are the input and back-reflected power, respectively. For the four situations we obtained similar values, i.e. $\eta_h = 41.9$ dB, $\eta_v = 41.3$ dB, $\eta_{45} = 41.9$ dB and $\eta_e = 40.6$ dB for horizontal, vertical, 45 deg and elliptical polarized inputs, respectively.

For evaluating the isolation capability of the PIOI we have to compare the forward power transmission $T_{1\to2}$ from port 1 to port 2 with the reverse power transmission $T_{2\to1}$ in backward direction. The isolation level is then defined as

$$\zeta(dB) = 10\log_{10}[T_{1\to2}/T_{2\to1}] \quad . \tag{7.1}$$

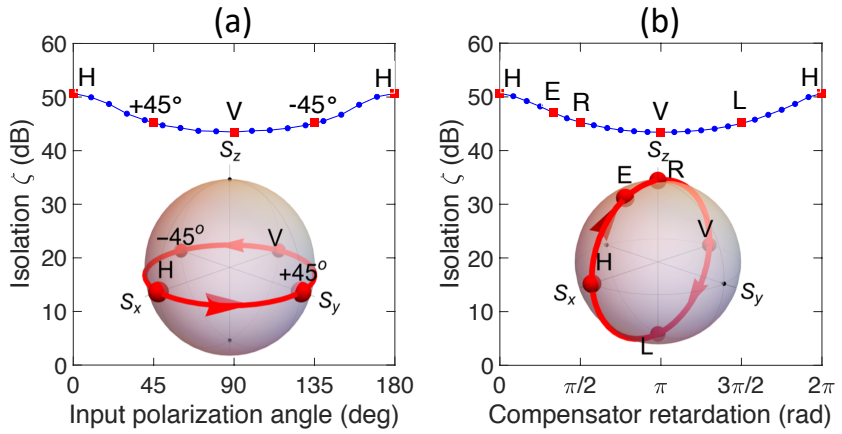

FIGURE 7.4: (Color online) Measured PIOI isolation ζ (dB) for various states of input polarization. In (a) all polarizations are linear and span the equator of the shown Poincaré sphere. In (b) they span a meridian line on the Poincaré sphere as obtained by varying the retardation of the input optical compensator. The labels H, V, +45°, −45°, E, R and L correspond to the horizontal, vertical, +45°,−45°, elliptical, right circular and left circular polarizations, respectively.

Figure 7.4 gives the measured isolation for different states of polarization. In Fig. 7.4(a) the polarization is linear and varies around the equator of the Poincaré sphere, as obtained by adjusting the compensator retardation to π (HWP) and rotating this element around the beam propagation axis. For Fig. 7.4(b), in contrast, the compensator has a fixed orientation at 45 deg but its retardation is varied between 0 and 2π at the used wavelength. This leads to a polarization variation along a meridian line on the Poincaré sphere, from horizontal (H) to various elliptical states (E), to right circular (R) and back to horizontal passing by the vertical (V) and the left circular state (L). As can be seen in Fig. 7.4 for all cases the isolation exceeds 43 dB and is larger than 50 dB for the horizontal polarization.

7.4 Conclusion

We have presented and verified experimentally an alternative concept for a polarization independent optical isolator. The fact that our scheme is based on a Sagnac-type ring interferometer brings about several advantages proper to common path interferometers. The most important one is the fact that there is no difference between the optical path of the two orthogonal polarizations, which allows to keep the polarization state between input and output. Also, such an arrangement features an increased robustness against length changes with respect to, for instance, Mach-Zehnder type isolators. Furthermore, the simple construction leads to easy tuning/adjustment. The implemented prototype was shown to conserve the input polarization state in forward direction and to provide an isolation exceeding 43 dB for all polarizations. We would like to mention that the use of two separated nonreciprocal polarization switches (and

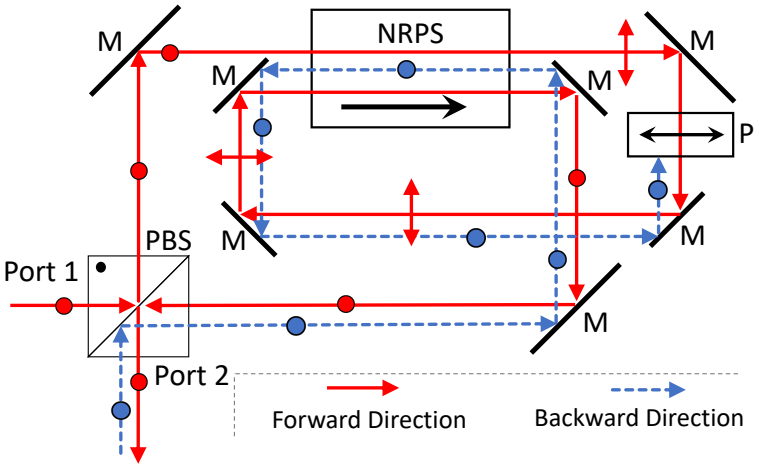

FIGURE 7.5: (Color online) Folded configuration using a double pass in a single NRPS, corresponding to the case of Fig. 7.2(a) (vertical input polarization). M: mirrors, all other symbols as in Fig. 7.2.

two Faraday rotators) is not strictly necessary. It is obviously possible to fold the optical path in such a way as to use the same NRPS twice as depicted in Fig. 7.5.

Chapter 8

Conclusions

Several aspects of the quantum-classical analogies between coherent quantum control strategies and specific classical systems were explored in this thesis. The primary goal of these analogies is to transmit concepts and techniques for successfully manipulating classical systems, making them robust and broadband, and demonstrating the profound relationship between these two seemingly contradictory worlds.

Coherent quantum control techniques, in general, are those that are used to efficiently and robustly manipulate multi-state quantum systems. In Chapter 2, we discussed the notion of Composite pulses (CPs) technique which is widely used to robustly manipulate two-state quantum systems. In addition, we discussed the manipulation of three-state quantum with a decaying intermediate state. In Chapter 3, we addressed the analogy between Composite pulses technique and the polarization manipulation in order to design robust and Broadband polarization rotator composed by three wave-plates. Another analogy based on using CPs in nonlinear optics is discussed in Chapter 4. In this chapter, a QPM-based nonlinear crystal is segmented by introducing defects in specific locations. This analogy aims to make the optical parametric amplification (OPA) robust and broadband. Chapter 5 presents the analogy between the population transfer in a three-state quantum system via a decaying state and the cascaded nonlinear frequency generation in a dissipative medium. This analogy allows rendering the absorption into advantage by stabilizing spatial powers along the nonlinear crystal.

Furthermore, for the first time, we designed a nonreciprocal wave retarder whose retardation depends on the light propagation direction. This device, discussed in Chapter 6, comprises a nonreciprocal polarization switch (NRPS) sandwiched between two crossed quarter-wave plates. Finally, in Chapter 7, we have discussed a polarization independent optical isolator composed by two NRPS in a Sagnac-type configuration. Such an isolator presented high isolation levels levels ranging from 43 dB to 50 dB.

Appendix A

Publications and Communications

A.1 Publications in Peer–Reviewed Journals

1. **Al-Mahmoud, Mouhamad**, Virginie Coda, Andon Rangelov, and Germano Montemezzani. "Broadband Polarization Rotator With Tunable Rotation Angle Composed of Three Wave Plates." *Physical Review Applied* **13**, no. 1 (2020): 014048.
   DOI: 10.1103/PhysRevApplied.13.014048

2. **Al-Mahmoud, Mouhamad**, Andon A. Rangelov, Virginie Coda, and Germano Montemezzani. "Segmented composite optical parametric amplification." *Applied Sciences* **10**, no. 4 (2020): 1220.
   DOI: 10.3390/app10041220

3. **Al-Mahmoud, Mouhamad**, Hristina Hristova, Virginie Coda, Andon A. Rangelov, Nikolay V. Vitanov and Germano Montemezzani. "Non-reciprocal wave retarder based on optical rotators combination." *OSA Continuum* **4**, 2695-2702 (2021).
   DOI: 10.1364/OSAC.439325

4. **Al-Mahmoud, Mouhamad**, Emiliya Dimova, Hristina Hristova, Virginie Coda, Andon A. Rangelov, and Germano Montemezzani. "Polarization-independent optical isolator in a Sagnac-type configuration." *Applied optics* **60**, no. 14 (2021): 4230-4234.
   DOI: 10.1364/AO.423730

5. Stoyanova, Elena, **Al-Mahmoud, Mouhamad**, Hristina Hristova, Andon Rangelov, Emiliya Dimova, and Nikolay V. Vitanov. "Achromatic polarization rotator with tunable rotation angle." *Journal of Optics* **21**, no. 10 (2019): 105403.
   DOI: 10.1088/2040-8986/ab40fc

A.2 International Conferences

1. **M. Al-Mahmoud**, V. Coda, A. A. Rangelov, and G. Montemezzani, "Application of Coherent Quantum Control Schemes in Classical Physics". MSCA-ITN: Light-Matter Interfaces for Quantum Enhanced Technologies, **LIMQUET-2021**, September 2021, Oxford, UK.

2. **M. Al-Mahmoud**, E. Dimova, E. Stojanova, V. Coda, A. A. Rangelov, N. V. Vitanov, and G. Montemezzani, "Nonlinear Frequency Generation In Dissipative System". La $8^{\grave{E}me}$ édition du congrès OPTIQUE de la SFO, **OPTIQUE-DIJON-2021**, July 2021, Dijon, France.

3. **M. Al-Mahmoud**, V. Coda, A. A. Rangelov, and G. Montemezzani, "Quasi-Phase Matching & Crystal Segmentation for Robust Optical Parametric Amplification". **CLEO/Europe-EQEC 2021** conference, June 2021, Virtual.

4. **M. Al-Mahmoud**, E. Dimova, E. Stojanova, V. Coda, A. A. Rangelov, N. V. Vitanov, and G. Montemezzani, "Quantum-Inspired Broadband Polarization Rotator". 2^{nd} International Conference on Optics and Photonics, **NICE CONFERENCE 2020**, October 2020, Nice, France.

5. **M. Al-Mahmoud**, V. Coda, A. A. Rangelov, and G. Montemezzani, "Broadband composite polarization rotators by using quantum control schemes". MSCA-ITN: Light-Matter Interfaces for Quantum Enhanced Technologies, **LIMQUET-2019**, September-2019, Nessebar, Bulgaria.

6. **M. Al-Mahmoud**, E. Dimova, V. Coda, A. A. Rangelov, and G. Montemezzani. "Design of new non-reciprocal wave retarder". The International Conference of Quantum, Nonlinear, and Nanophotonics, **ICQNN-2019**, September 2019, Sofia, Bulgaria.

7. **M. Al-Mahmoud**, E. Dimova, V. Coda, A. A. Rangelov, N. V. Vitanov, and G. Montemezzani. "Method to realize a non-reciprocal wave retarder". The Seventh International School and Conference on Photonics & Machine Learning with Photonics Symposium, **PHOTONICA-2019**, August 2019, Belgrade, Serbia.

8. **M. Al-Mahmoud**, E. Dimova, V. Coda, A. A. Rangelov, and G. Montemezzani. "Non-reciprocal wave plate". Control of Quantum Dynamics of Atoms, Molecules, and Ensembles by Light, **CAMEL-XV**, June 2019, Nessebar, Bulgaria.

A.3 Seminars

1. **M. Al-Mahmoud**, V. Coda, A. A. Rangelov, and G. Montemezzani, "Application des Techniques de Contrôle Quantique Cohérent en Optique". Séminaire journée des doctorants, **JDD-2021**, June 2021, MOPS Laboratory, Metz, France.

2. **M. Al-Mahmoud**, V. Coda, A. A. Rangelov, and G. Montemezzani, "Quantum-classical Analogy for Broadband Classical Systems". Seminar of theoretical physics department, **Group of Quantum Optics & Quantum Information** March 2021, Sofia, Bulgaria.

3. **M. Al-Mahmoud**, V. Coda, A. A. Rangelov, and G. Montemezzani, "Amplification paramétrique optique par cristal segmenté". Séminaire journée des doctorants, **JDD-2020**, June 2020, MOPS Laboratory, Metz, France.

4. **M. Al-Mahmoud**, V. Coda, A. A. Rangelov, and G. Montemezzani, "Rotateurs de polarization robuste et large-bande basée sur l'analogie Quantique-Optique." Séminaire journée des doctorants, **JDD-2019**, June 2019, MOPS Laboratory, Metz, France.

Bibliography

[1] Daniela Dragoman and Mircea Dragoman. *Quantum-classical analogies*. Springer Science & Business Media, 2013.

[2] Malcolm H Levitt. "Composite pulses". In: *Progress in Nuclear Magnetic Resonance Spectroscopy* 18.2 (1986), pp. 61–122.

[3] R. Freeman. *Spin Choreography: Basic Steps in High Resolution NMR*. Spektrum, 1997. ISBN: 978-1-901217-04-9.

[4] Stephen Wimperis. "Broadband, narrowband, and passband composite pulses for use in advanced NMR experiments". In: *Journal of Magnetic Resonance, Series A* 109.2 (1994), pp. 221–231.

[5] Neeraj Sinha, Klaus Schmidt-Rohr, and Mei Hong. "Compensation for pulse imperfections in rotational-echo double-resonance NMR by composite pulses and EXORCYCLE". In: *Journal of Magnetic Resonance* 168.2 (2004), pp. 358–365.

[6] DJ Siminovitch et al. "Composite pulse excitation in quadrupole echo spectroscopy". In: *The Journal of chemical physics* 84.5 (1986), pp. 2556–2565.

[7] Svetoslav S Ivanov and Nikolay V Vitanov. "High-fidelity local addressing of trapped ions and atoms by composite sequences of laser pulses". In: *Optics letters* 36.7 (2011), pp. 1275–1277.

[8] Boyan T Torosov, Stéphane Guérin, and Nikolay V Vitanov. "High-fidelity adiabatic passage by composite sequences of chirped pulses". In: *Physical review letters* 106.23 (2011), p. 233001.

[9] Martin Weitz, Brenton C Young, and Steven Chu. "Atomic interferometer based on adiabatic population transfer". In: *Physical review letters* 73.19 (1994), p. 2563.

[10] P Marte, P Zoller, and John L Hall. "Coherent atomic mirrors and beam splitters by adiabatic passage in multilevel systems". In: *Physical Review A* 44.7 (1991), R4118.

[11] Thomas Zanon-Willette et al. "Composite pulses in Hyper-Ramsey spectroscopy for the next generation of atomic clocks". In: *Journal of Physics: Conference Series*. Vol. 723. 1. IOP Publishing. 2016, p. 012057.

[12] Lori S Goldner et al. "Momentum transfer in laser-cooled cesium by adiabatic passage in a light field". In: *Physical review letters* 72.7 (1994), p. 997.

[13] Genko T Genov et al. "Correction of arbitrary field errors in population inversion of quantum systems by universal composite pulses". In: *Physical review letters* 113.4 (2014), p. 043001.

[14] Li Gengying, Wang Dongsheng, and Wu Xuewen. "Composite pulse magic echo sequence in three-level systems". In: *Review of scientific instruments* 59.4 (1988), pp. 569–572.

[15] Hartmut Häffner, Christian F Roos, and Rainer Blatt. "Quantum computing with trapped ions". In: *Physics reports* 469.4 (2008), pp. 155–203.

[16] Svetoslav S Ivanov and Nikolay V Vitanov. "Scalable uniform construction of highly conditional quantum gates". In: *Physical Review A* 84.2 (2011), p. 022319.

[17] Xin Wang et al. "Composite pulses for robust universal control of singlet–triplet qubits". In: *Nature communications* 3.1 (2012), pp. 1–7.

[18] William G Alway and Jonathan A Jones. "Arbitrary precision composite pulses for NMR quantum computing". In: *Journal of Magnetic Resonance* 189.1 (2007), pp. 114–120.

[19] Charles H Bennett and David P DiVincenzo. "Quantum information and computation". In: *nature* 404.6775 (2000), pp. 247–255.

[20] HK Cummins and JA Jones. "Use of composite rotations to correct systematic errors in NMR quantum computation". In: *New Journal of Physics* 2.1 (2000), p. 6.

[21] Holly K Cummins, Gavin Llewellyn, and Jonathan A Jones. "Tackling systematic errors in quantum logic gates with composite rotations". In: *Physical Review A* 67.4 (2003), p. 042308.

[22] John JL Morton et al. "High fidelity single qubit operations using pulsed electron paramagnetic resonance". In: *Physical review letters* 95.20 (2005), p. 200501.

[23] E Collin et al. "NMR-like control of a quantum bit superconducting circuit". In: *Physical review letters* 93.15 (2004), p. 157005.

[24] Robert W. Boyd. *Nonlinear optics (Third Edition)*. Third Edition. Burlington: Academic Press, 2008. ISBN: 978-0-12-369470-6.

[25] Y.R. Shen. *The Principles of Nonlinear Optics*. Wiley classics library. Wiley, 2003. ISBN: 978-0-471-43080-3.

[26] R. M. A. Azzam and N. M. Bashara. *Ellipsometry and polarized light*. Amsterdam: North-Holland, 1987. ISBN: 0-444-87016-4 978-0-444-87016-2.

[27] David N Nikogosyan. *Nonlinear optical crystals: a complete survey*. Springer Science & Business Media, 2006.

[28] Frits Zernike and John E Midwinter. *Applied nonlinear optics*. New York: Wiley, 1973.

[29] Boyan T Torosov and Nikolay V Vitanov. "Smooth composite pulses for high-fidelity quantum information processing". In: *Physical Review A* 83.5 (2011), p. 053420.

[30] Bruce W Shore. *The theory of coherent atomic excitation*. New York: Wiley, 1990.

[31] Daniel Zeuch et al. "Exact rotating wave approximation". In: *Annals of physics* 423 (2020), p. 168327.

[32] Kazuyuki Fujii. "Introduction to the rotating wave approximation (rwa): Two coherent oscillations". In: *arXiv preprint arXiv:1301.3585* (2013).

[33] Felix Klein. *The Mathematical Theory of the Top: Lectures Delivered on the Occasion of the Sesquicentennial Celebration of Princeton University*. C. Scribner's sons, 1897.

[34] NV Vitanov and Stig Stenholm. "Population transfer via a decaying state". In: *Physical Review A* 56.2 (1997), p. 1463.

[35] NV Vitanov and Stig Stenholm. "Properties of stimulated Raman adiabatic passage with intermediate-level detuning". In: *Optics communications* 135.4-6 (1997), pp. 394–405.

[36] Dennis H Goldstein and Edward Collett. *Polarized light*. New York: Marcel Dekker, 2003. ISBN: 978-0-8247-4053-5.

[37] Francisco Javier Duarte. *Tunable Laser Optics*. CRC Pr I Llc, 2017. ISBN: 978-1-138-89375-7 978-1-4822-4529-5.

[38] David S Kliger and James W Lewis. *Polarized light in optics and spectroscopy*. Elsevier, 2012.

[39] CD West and AS Makas. "The spectral dispersion of birefringence, especially of birefringent plastic sheets". In: *JOSA* 39.9 (1949), pp. 791–794.

[40] G Destriau and J Prouteau. "Réalisation d'un quart d'onde quasi achromatique par juxtaposition de deux lames cristallines de même nature". In: *Journal de Physique et le Radium* 10.2 (1949), pp. 53–55.

[41] Shivaramakrishnan Pancharatnam. "Achromatic combinations of birefringent plates". In: *Proceedings of the Indian Academy of Sciences-Section A*. Vol. 41. 4. Springer. 1955, pp. 130–136.

[42] Shivaramakrishnan Pancharatnam. "Achromatic combinations of birefringent plates". In: *Proceedings of the Indian Academy of Sciences-Section A*. Vol. 41. 4. Springer. 1955, pp. 137–144.

[43] Charles Moore McIntyre and SE Harris. "Achromatic wave plates for the visible spectrum". In: *JOSA* 58.12 (1968), pp. 1575–1580.

[44] Arzhang Ardavan. "Exploiting the Poincaré–Bloch symmetry to design high-fidelity broadband composite linear retarders". In: *New Journal of Physics* 9.2 (2007), p. 24.

[45] Svetoslav S Ivanov et al. "Highly efficient broadband conversion of light polarization by composite retarders". In: *JOSA A* 29.3 (2012), pp. 265–269.

[46] Thorsten Peters et al. "Variable ultrabroadband and narrowband composite polarization retarders". In: *Applied optics* 51.31 (2012), pp. 7466–7474.

[47] E St Dimova et al. "Highly efficient broadband polarization retarders and tunable polarization filters made of composite stacks of ordinary wave plates". In: *JOSA A* 31.5 (2014), pp. 952–956.

[48] Emiliya Dimova et al. "Broadband and ultra-broadband modular half-wave plates". In: *Optics Communications* 366 (2016), pp. 382–385.

[49] Andon A. Rangelov and Elica Kyoseva. "Broadband composite polarization rotator". In: *Optics Communications* 338 (Mar. 2015), pp. 574–577.

[50] Emiliya Dimova, Andon Rangelov, and Elica Kyoseva. "Tunable bandwidth optical rotator". In: *Photon. Res.* 3.4 (Aug. 2015), pp. 177–179.

[51] Elena Stoyanova et al. "Achromatic polarization rotator with tunable rotation angle". In: *Journal of Optics* 21.10 (2019), p. 105403.

[52] W Joosen et al. "Broadband femtosecond infrared parametric amplification in β-BaB 2 O 4". In: *Optics letters* 17.2 (1992), pp. 133–135.

[53] GM Gale et al. "Sub-20-fs tunable pulses in the visible from an 82-MHz optical parametric oscillator". In: *Optics letters* 20.14 (1995), pp. 1562–1564.

[54] GM Gale, F Hache, and M Cavallari. "Broad-bandwidth parametric amplification in the visible: femtosecond experiments and simulations". In: *IEEE Journal of selected topics in quantum electronics* 4.2 (1998), pp. 224–229.

[55] Bruno E Schmidt et al. "Frequency domain optical parametric amplification". In: *Nature communications* 5.1 (2014), pp. 1–8.

[56] Malcolm H Levitt and Ray Freeman. "NMR population inversion using a composite pulse". In: *Journal of Magnetic Resonance (1969)* 33.2 (1979), pp. 473–476.

[57] AJ Shaka. "Composite pulses for ultra-broadband spin inversion". In: *Chemical physics letters* 120.2 (1985), pp. 201–205.

[58] AJ Shaka and A Pines. "Symmetric phase-alternating composite pulses". In: *Journal of Magnetic Resonance (1969)* 71.3 (1987), pp. 495–503.

[59] A Dubietis, G Jonušauskas, and A Piskarskas. "Powerful femtosecond pulse generation by chirped and stretched pulse parametric amplification in BBO crystal". In: *Optics Communications* 88.4-6 (1992), pp. 437–440.

[60] Audrius Dubietis, Rytis Butkus, and Algis Petras Piskarskas. "Trends in chirped pulse optical parametric amplification". In: *IEEE Journal of selected topics in quantum electronics* 12.2 (2006), pp. 163–172.

[61] Yunpei Deng et al. "Carrier-envelope-phase-stable, 1.2 mJ, 1.5 cycle laser pulses at 2.1 μm". In: *Optics letters* 37.23 (2012), pp. 4973–4975.

[62] György Tóth et al. "Scalable broadband OPCPA in Lithium Niobate with signal angular dispersion". In: *Optics Communications* 370 (2016), pp. 250–255.

[63] Amnon Yariv and Pochi Yeh. *Photonics: optical electronics in modern communications*. Oxford University Press, 2007.

[64] R Baumgartner and R Byer. "Optical parametric amplification". In: *IEEE Journal of Quantum Electronics* 15.6 (1979), pp. 432–444.

[65] *Jacobi Elliptic Functions@ONLINE*. Accessed: 2021-09-09. Sept. 2021. URL: http://mathworld.wolfram.com/JacobiEllipticFunctions.html.

[66] Ferdinand Schmidt-Kaler et al. "Realization of the Cirac–Zoller controlled-NOT quantum gate". In: *Nature* 422.6930 (2003), pp. 408–411.

[67] N Timoney et al. "Error-resistant single-qubit gates with trapped ions". In: *Physical Review A* 77.5 (2008), p. 052334.

[68] Daniel Schraft et al. "Experimental demonstration of composite adiabatic passage". In: *Physical Review A* 88.6 (2013), p. 063406.

[69] Florian Bach et al. "Laser induced damage studies of LiNbO 3 using 1030-nm, ultrashort pulses at 10-1000 kHz". In: *Optical Materials Express* 7.1 (2017), pp. 240–252.

[70] Qinglong Meng et al. "Damage threshold of lithium niobate crystal under single and multiple femtosecond laser pulses: theoretical and experimental study". In: *Applied Physics A* 122.6 (2016), p. 582.

[71] Hassan Oukraou et al. "Control of adiabatic light transfer in coupled waveguides with longitudinally varying detuning". In: *Physical Review A* 95.2 (2017), p. 023811.

[72] Mouhamad Al-Mahmoud et al. "Broadband polarization rotator with tunable rotation angle composed of three wave plates". In: *Physical Review Applied* 13.1 (2020), p. 014048.

[73] Mouhamad Al-Mahmoud et al. "Segmented composite optical parametric amplification". In: *Applied Sciences* 10.4 (2020), p. 1220.

[74] Gil Porat and Ady Arie. "Efficient two-process frequency conversion through a dark intermediate state". In: *JOSA B* 29.10 (2012), pp. 2901–2909.

[75] Pragati Aashna and K Thyagarajan. "Cascaded frequency conversion under nonlinear stimulated Raman adiabatic passage". In: *Optics Letters* 46.7 (2021), pp. 1486–1489.

[76] Fujie Li et al. "Synthesis of white laser source based on nonlinear frequency conversion with stimulated Raman adiabatic passage". In: *Optics Communications* 502 (2022), p. 127427.

[77] Gil Porat et al. "Two photon frequency conversion". In: *Optics express* 20.4 (2012), pp. 3613–3619.

[78] Paul N Butcher and David Cotter. *The elements of nonlinear optics*. 9. Cambridge university press, 1990.

[79] JA Armstrong et al. "Interactions between light waves in a nonlinear dielectric". In: *Physical review* 127.6 (1962), p. 1918.

[80] Martin M Fejer et al. "Quasi-phase-matched second harmonic generation: tuning and tolerances". In: *IEEE Journal of quantum electronics* 28.11 (1992), pp. 2631–2654.

[81] Robert L Byer. "New material for high average power infrared generation: QPM-DB GaAs". In: *Stanford Univ. Report* (1994).

[82] David S Hum and Martin M Fejer. "Quasi-phasematching". In: *Comptes Rendus Physique* 8.2 (2007), pp. 180–198.

[83] Wenjie Wang et al. "Third-harmonic generation via broadband cascading in disordered quadratic nonlinear media". In: *Optics Express* 17.22 (2009), pp. 20117–20123.

[84] MH Chou et al. "1.5-μm-band wavelength conversion based on cascaded second-order nonlinearity in LiNbO 3 waveguides". In: *IEEE Photonics Technology Letters* 11.6 (1999), pp. 653–655.

[85] Junqiang Sun et al. "Wavelength conversion between picosecond pulses using cascaded second-order nonlinearity in LiNbO 3 waveguides". In: *Optical and quantum electronics* 37.5 (2005), pp. 443–456.

[86] Yeung Lak Lee et al. "All-optical wavelength conversion and tuning by the cascaded sum-and difference frequency generation (cSFG/DFG) in a temperature gradient controlled Ti: PPLN channel waveguide". In: *Optics Express* 13.8 (2005), pp. 2988–2993.

[87] Jian Wang et al. "Experimental demonstration of wavelength conversion between ps-pulses based on cascaded sum-and difference frequency generation (SFG+ DFG) in LiNbO 3 waveguides". In: *Optics Express* 13.19 (2005), pp. 7405–7414.

[88] Jian Wang et al. "Tunable wavelength conversion of ps-pulses exploiting cascaded sum-and difference frequency generation in a PPLN-fiber ring laser". In: *IEEE photonics technology letters* 18.20 (2006), pp. 2093–2095.

[89] Bo Chen and Chang-Qing Xu. "Analysis of novel cascaded $\chi^{(2)}$ (SFG+DFG) wavelength conversions in quasi-phase-matched waveguides". In: *IEEE journal of quantum electronics* 40.3 (2004), pp. 256–261.

[90] Song Yu and Wanyi Gu. "Wavelength conversions in quasi-phase matched $LiNbO_3$ waveguide based on double-pass cascaded $\chi^{(2)}$ SFG+ DFG interactions". In: *IEEE Journal of Quantum electronics* 40.11 (2004), pp. 1548–1554.

[91] Jian Wang et al. "Experimental observation of tunable wavelength down-and up-conversions of ultra-short pulses in a periodically poled LiNbO3 waveguide". In: *Optics communications* 269.1 (2007), pp. 179–187.

[92] Hideaki Furukawa et al. "Tunable all-optical wavelength conversion of 160-Gb/s RZ optical signals by cascaded SFG-DFG generation in PPLN waveguide". In: *IEEE Photonics Technology Letters* 19.6 (2007), pp. 384–386.

[93] Y Wang, B Chen, and C-Q Xu. "Polarisation-insensitive QPM wavelength converter with out-of-band pump". In: *Electronics Letters* 40.3 (2004), pp. 189–191.

[94] Song Yu and Wanyi Gu. "A tunable wavelength conversion and wavelength add/drop scheme based on cascaded second-order nonlinearity with double-pass configuration". In: *IEEE journal of quantum electronics* 41.7 (2005), pp. 1007–1012.

[95] Shiming Gao et al. "Performance evaluation of tunable channel-selective wavelength shift by cascaded sum-and difference-frequency generation in periodically poled lithium niobate waveguides". In: *Journal of lightwave technology* 25.3 (2007), pp. 710–718.

[96] JE McGeehan, M Giltrelli, and AE Willner. "All-optical digital 3-input AND gate using sum-and difference-frequency generation in PPLN waveguide". In: *Electronics Letters* 43.7 (2007), pp. 409–410.

[97] Jian Wang, Junqiang Sun, and Qizhen Sun. "Single-PPLN-based simultaneous half-adder, half-subtracter, and OR logic gate: proposal and simulation". In: *Optics express* 15.4 (2007), pp. 1690–1699.

[98] Jian Wang, Junqiang Sun, and Qizhen Sun. "Proposal for all-optical switchable OR/XOR logic gates using sum-frequency generation". In: *IEEE Photonics Technology Letters* 19.8 (2007), pp. 541–543.

[99] Amirhossein Tehranchi and Raman Kashyap. "Response flattening of efficient broadband wavelength converters based on cascaded sum and difference frequency generation in periodically poled lithium niobate waveguides". In: *IEEE journal of quantum electronics* 45.9 (2009), pp. 1114–1120.

[100] Antonella Bogoni et al. "Photonic processing of 320 Gbits/s based on sum-/difference-frequency generation and pump depletion in a single PPLN waveguide". In: *Optics letters* 34.12 (2009), pp. 1825–1827.

[101] Sylvain D Gennaro et al. "Cascaded Third Harmonic Generation in Dielectric Metasurfaces". In: *CLEO: Science and Innovations*. Optical Society of America. 2020, JTh2E–24.

[102] Miriam Carrillo-Fuentes et al. "Sub-nanosecond terahertz radiation obtained with an aperiodically poled lithium niobate and organic HMQ-TMS". In: *Optics Express* 28.17 (2020), pp. 24444–24451.

[103] Eugene Hecht. *Optics*. 2017. ISBN: 978-1-292-09693-3.

[104] R. J. Potton. "Reciprocity in optics". In: *Rep. Prog. Phys.* 67 (2004), pp. 717–754.

[105] Dirk Jalas et al. "What is - and what is not - an optical isolator". In: *Nature Photonics* 7 (2013), pp. 579–582.

[106] M. Z. Zha and P. Günter. "Nonreciprocal optical transmission through photorefractive $KNbO_3$:Mn". In: *Opt. Lett* 10 (1985), pp. 184–186.

[107] K. A. Stankov, V. P. Tzolov, and M. G. Mirkov. "Nonreciprocal optical device based on second-harmonic generation". In: *Appl. Opt.* 31 (1992), pp. 5003–5009.

[108] K. Gallo et al. "All-optical diode in a periodically poled lithium niobate waveguide". In: *Appl. Phys. Lett.* 79 (2001), pp. 314–316.

[109] I. O. Zolotovskii and D. I. Sementsov. "Nonreciprocal effects in active nonlinear optical fibers with nonlinearity dispersion". In: *Opt. Spectr.* 101 (2006), pp. 446–449.

[110] M. Krause, H. Renner, and E. Brinkmeyer. "Optical isolation in silicon waveguides based on nonreciprocal Raman amplification". In: *Electron. Lett.* 44 (2008), pp. 691–693.

[111] Z. Yu and S. Fan. "Complete optical isolation created by indirect interband photonic transitions". In: *Nature Photonics* 3 (2009), pp. 91–94.

[112] R. Fleury, D. L. Sounas, and A. Alù. "Non-reciprocal optical mirrors based on spatio-temporal acousto-optic modulation". In: *J. Opt.* 20 (2018), p. 034007.

[113] J. Wang, Y. Shi, and S. Fan. "Non-reciprocal polarization rotation using dynamic refractive index modulation". In: *Opt. Express* 28 (2020), pp. 11974–11982.

[114] M. A. Nielsen and I. L. Chuang. *Quantum Computation and Quantum Information*. Cambridge University Press, Cambridge, 2000.

[115] J. C. Suits, B. E. Argyle, and M. J. Freiser. "Magneto-optical properties of materials containing divalent Europium". In: *J. Appl. Phys.* 37 (1966), pp. 1391–1397.

[116] V. Vasyliev et al. "UV-visible Faraday rotators based on rare-earth fluoride single crystals: $LiREF_4$ (RE = Tb, Dy, Ho, Er and Yb), PrF_3 and CeF_3". In: *Opt. Express* 20 (2012), pp. 14460–14470.

[117] M. Al-Mahmoud, V. Coda, A. A. Rangelov and G. Montemezzani. "Broadband polarization rotator with tunable rotation angle composed of three wave plates". In: *Phys. Rev. Applied* 13 (2020), p. 014048.

[118] Lord Rayleigh. "On the Constant of Magnetic Rotation of Light in Bisulphide of Carbon". In: *Phil. Trans. R. Soc. London* 176 (1885), pp. 343–366.

[119] B. J. H. Stadler and T. Mizumoto. "Integrated Magneto-Optical Materials and Isolators: A Review". In: *IEEE Photonics Journal* 6 (2014), pp. 1–15.

[120] Duanni Huang et al. "Integrated broadband Ce:YIG/Si Mach-Zehnder optical isolators with over 100 nm tuning range". In: *Opt. Lett.* 42 (2017), pp. 4901–4904.

[121] Paolo Pintus et al. "Broadband TE optical isolators and circulators in silicon photonics through Ce:YIG bonding". In: *Journal of Lightwave Technology* 37.5 (2019), pp. 1463–1473.

[122] Karthik Srinivasan et al. "High-Gyrotropy Seedlayer-Free Ce:TbIG for Monolithic Laser-Matched SOI Optical Isolators". In: *ACS Photonics* 6 (2019), pp. 2455–2461.

[123] Wei Yan et al. "Waveguide-integrated high-performance magneto-optical isolators and circulators on silicon nitride platforms". In: *Optica* 7.11 (2020), pp. 1555–1562.

[124] K Nakajima, Y Numajiri, and Y Nomi. "New design of a polarization-independent optical isolator with high performance". In: *IEEE Trans. Magn.* 27.6 (1991), pp. 5399–5401.

[125] K Shiraishi. "New configuration of polarisation-independent isolator using a polarisation-dependent one". In: *Electron. Lett.* 27.4 (1991), pp. 302–303.

[126] Kok Wai Chang and WW Sorin. "Polarization independent isolator using spatial walkoff polarizers". In: *IEEE Photonics Technology Letters* 1.3 (1989), pp. 68–70.

[127] Kok Wai Chang and Wayne V. Sorin. "High-performance single-mode fiber polarization-independent isolators". In: *Opt. Lett.* 15 (1990), pp. 449–451.

[128] O. Zhuromskyy et al. "Analysis of Polarization Independent Mach-Zehnder-Type Integrated Optical Isolator". In: *J. Lightwave Technol.* 17.7 (1999), pp. 1200–1205.

[129] J. Fujita et al. "Polarization-independent waveguide optical isolator based on nonreciprocal phase shift". In: *IEEE Photonics Technology Letters* 12.11 (2000), pp. 1510–1512.

[130] Y. Shoji et al. "Polarization-independent magneto-optical waveguide isolator using TM-mode nonreciprocal phase shift". In: *J. Lightwave Technol.* 25.10 (2007), pp. 3108–3113.

[131] Iwamura Hidetoshi et al. "Simple polarisation-independent optical circulator for optical transmission systems". In: *Electronics Letters* 15.25 (1979), pp. 830–831.

[132] Takao Matsumoto and Ken Ichi Sato. "Polarization-independent optical circulator: an experiment". In: *Applied Optics* 19.1 (1980), pp. 108–112.

[133] W. Emkey. "A polarization-independent optical circulator for 1.3 μm". In: *Journal of Lightwave Technology* 1 (1983), pp. 466–469.

[134] Masataka Shirasaki, Hideo Kuwahara, and Takeshi Obokata. "Compact polarization-independent optical circulator". In: *Applied Optics* 20.15 (1981), pp. 2683–2687.

[135] Xuejin Yan and Shangqing Xiao. "Magneto-optic circulator for optical fiber transmission". In: *Journal Applied Physics* 65.4 (1989), pp. 1664–1665.

[136] Yohji Fujii. "High-isolation polarization-independent optical circulator coupled with single-mode fibers". In: *Journal Lightwave Technology* 9.4 (1991), pp. 456–460.

[137] Yohji Fujii. "High-isolation polarization-independent optical circulator". In: *Journal of Lightwave Technology* 9.10 (1991), pp. 1238–1243.

[138] M. Koga and T. Matsumoto. "High-isolation polarization-insensitive optical circulator for advanced optical communication systems". In: *Journal of Lightwave Technology* 10 (1992), pp. 1210–1217.

[139] Lin Dou Wang. "High-isolation polarization-independent optical quasi-circulator with a simple structure". In: *Optics Letters* 23.7 (1998), pp. 549–551.

[140] Jing Heng Chen, Der Chin Su, and Jung Chieh Su. "Holographic spatial walk-off polarizer and its application to a 4-port polarization-independent optical circulator". In: *Optics Express* 11.17 (2003), pp. 2001–2006.

[141] N Sugimoto et al. "Waveguide polarization-independent optical circulator". In: *IEEE Photonics Technology Letters* 11.3 (1999), pp. 355–357.

[142] T. R. Zaman, X. Guo, and R. J. Ram. "Proposal for a polarization-independent integrated optical circulator". In: *IEEE Photonics Technology Letters* 18.12 (2006), pp. 1359–1361.

[143] Curtis J. Firby et al. "Versatile broadband polarization-independent optical circulators for nanophotonic integrated circuits". In: *J. Opt. Soc. Am. B* 35.7 (2018), pp. 1504–1513.